DETERMINING THE SUPERCONDUCTING ORDER PARAMETER OF UPt_3 WITH JOSEPHSON JUNCTION INTERFEROMETRY

BY

JOEL D. STRAND

DISSERTATION

Submitted in partial fulfillment of the requirements
for the degree of Doctor of Philosophy in Physics
in the Graduate College of the
University of Illinois at Urbana-Champaign, 2010

Urbana, Illinois

Doctoral Committee:

Professor Lance Cooper, Chair
Professor Dale Van Harlingen, Advisor
Professor Michael Stone
Professor Kevin Pitts

Abstract

We report evidence for a complex low-temperature superconducting phase in UPt_3 that breaks time-reversal symmetry and exhibits a phase shift of π in the superconducting order parameter between the a- and b-axes. We also report evidence for nodes in the amplitude of the superconducting energy gap in the high-temperature phase of UPt_3. These nodes occur 45° between the a- and b-axes and fill in as an out-of-phase energy gap component develops. This evidence supports the E_{2u} representation of the superconducting order parameter. These measurements were taken by fabricating Pb–Cu–UPt_3 Josephson junctions on polished and as-grown surfaces of UPt_3 single crystals. By measuring the critical current through the junctions and varying the applied magnetic field, temperature, and angle of the junctions, we obtained information on the phase and magnitude of the superconducting order parameter.

To my wife Natalie,
for making my time in graduate school more wonderful
than I ever hoped it could be.

Acknowledgments

I would like to thank my advisor Dale Van Harlingen for being an outstanding teacher and scientist. It has been a pleasure to be a part of his research group. His care for his students was always evident, and I learned an incredible amount under his direction. I would like to thank all the members of the DVH research group for making our lab such a friendly and helpful place; I can't imagine a better environment in which to perform research. In particular, I would like to thank Francoise Kidwingira for mentoring me when I first joined the group and teaching me so many of the techniques that I used during my time at UIUC. I would also like to thank Micah Stoutimore and Daniel Bahr for their friendship, conversation, and assistance whenever I needed them.

Thanks also go to William Halperin and his group at Northwestern University. Dr. Halperin has been an amazing collaborator, and his attentiveness and engagement at all stages of our work were invaluable. I also appreciate the work that William Gannon and the rest of the crystal growing team did in providing me with the best UPt_3 samples in the world.

The love of my family has been a constant source of strength for me, and I want to thank my parents Jerry and Kathy Strand, my sister Kara, and most of all my wife Natalie for providing me with so much support.

Most importantly, I praise God for blessing me with the ability and opportunity to glorify Him by studying the intricacies of His amazing creation.

Lastly, this work would not have been possible without the support of the funding agencies and the facilities of the Frederick Seitz Materials Research Laboratory. The work at the University of Illinois at Urbana-Champaign was supported by NSF grant DMR07-05214. The work at Northwestern University was supported by the DOE Basic Energy Sciences grant DE-FG02-05ER46248.

Table of Contents

Chapter 1

Introduction

The phenomenon of superconductivity has been an active area of research for physicists since its first observation by Kamerlingh Onnes almost a century ago[1]. Characterized by lossless current flow and perfect diamagnetism, superconductivity both fascinated and confounded physicists for nearly fifty years before two separate approaches achieved success in providing explanations for this behavior.

The first was a phenomenological approach developed by Ginzburg and Landau out of a general theory of phase transitions by Landau[2]. Their theory focused on how the free energy of the superconductor varied with position or in a field, and they introduced an order parameter, Ψ, to characterize the superconducting state. They also introduced two characteristic length scales: the penetration depth, λ, which defines the depth that magnetic field penetrates into the superconductor, and the coherence length, ξ, which defines the length over which changes in Ψ occur. One advantage of their theory is that it is very general and does not depend on any particular microscopic model, allowing it to be applied to materials such as the high T_C cuprate superconductors where the microscopic mechanism of superconductivity is not understood.

The second approach was a theory developed by Bardeen, Cooper, and Schrieffer in 1957[3]. The BCS theory, as it is known, considered how electrons near the Fermi surface could form pairs under an attractive potential.

They considered an attraction mediated by phonons polarizing the crystal lattice, but other attractive mechanisms can also lead to superconductivity. Under this attractive potential, the electrons form what are called Cooper pairs and condense into a single groundstate, where they share a wavefunction that preserves phase coherence over the entire system. This groundstate is separated from excitations by an energy gap that forms on either side of the Fermi surface. This energy gap, which can be shown to be proportional to the Ginzburg-Landau order parameter[4], is isotropic in amplitude and consists of a single phase. The BCS theory was amazingly successful in explaining the properties of the superconductors known at the time, and remains a great triumph for theoretical physics.

Since that time, however, the field of superconductivity has started to confound physicists again. Numerous unconventional superconductors that cannot be explained by the BCS model have been discovered in recent decades, most noticeably the high temperature copper oxide superconductors which have transition temperatures well above the boiling point of nitrogen. New uses for superconductors such as quantum computing have also emerged in recent years. These discoveries have opened up new technological possibilities and sparked renewed interest in the field.

Unconventional superconductivity is exciting because it shows that the BCS model is not a unique solution to the phenomenon of superconductivity, and that there are many ways to achieve a superconducting state. The more we understand about unconventional superconductivity the more ways we will find to create and optimize superconductors, hopefully culminating in useful materials at conveniently accessible temperatures. One of the most interesting of these new superconductors is UPt_3, which was the first unconventional superconductor, discovered even before the high temperature

superconductors, and which will be the topic of this study.

In Chapter 2 we will present a summary of the properties of UPt_3 that make it so interesting to study and a description of the theories that have been proposed to describe it. Chapter 3 contains an introduction to the Josephson effect and an overview of the technique of Josephson interferometry that we will use to probe the superconducting order parameter. Chapter 4 describes how our samples are made and the equipment used for our measurements. In Chapter 5 we present our data on phase-sensitive measurements and evidence for a complex low-temperature phase that breaks time-reversal symmetry and in Chapter 6 we present data on the temperature dependence of junction critical currents as a function of angle, which shows the location of a node in the energy gap and the transition between two superconducting phases.

Chapter 2

Properties of UPt_3

2.1 Overview

At almost all temperatures UPt_3 is a relatively normal metal. It has a close-packed hexagonal structure with lattice parameters $a = 5.712$ Å and $c = 4.864$ Å that can be distorted into a trigonal lattice under pressure[5]. The b-axis is conventionally defined as perpendicular to the a-axis in this system, rather than at 30°. A picture of the crystal lattice is shown in Figure 2.1.

It exhibits Fermi liquid behavior and has nearly isotropic conductivity. It was first studied because it falls into a class of metals known as heavy fermion conductors. The name came about because the conduction electrons in these materials behave as though their masses were substantially greater than the electron mass. The source of this behavior in UPt_3 are the U $5f$ electrons, which only partially fill the band, and their uncanceled spins act as internal magnetic moments. The conduction band electrons act to screen these moments, and that interaction makes them less responsive to other stimuli, which gives them an effective mass of $m^* = 187m_e$[6].

Superconductivity was first discovered in UPt_3 by Stewart et. al. in 1984[8]. The initial transition temperature was measured at $540mK$. The coherence length for UPt_3 is $12nm$[6], and the penetration depth is $700nm$[9]. There is also evidence from neutron diffraction that there is a weak antiferromagnetic moment in the basal plane, $T_N = 5K$[10], that coexists with

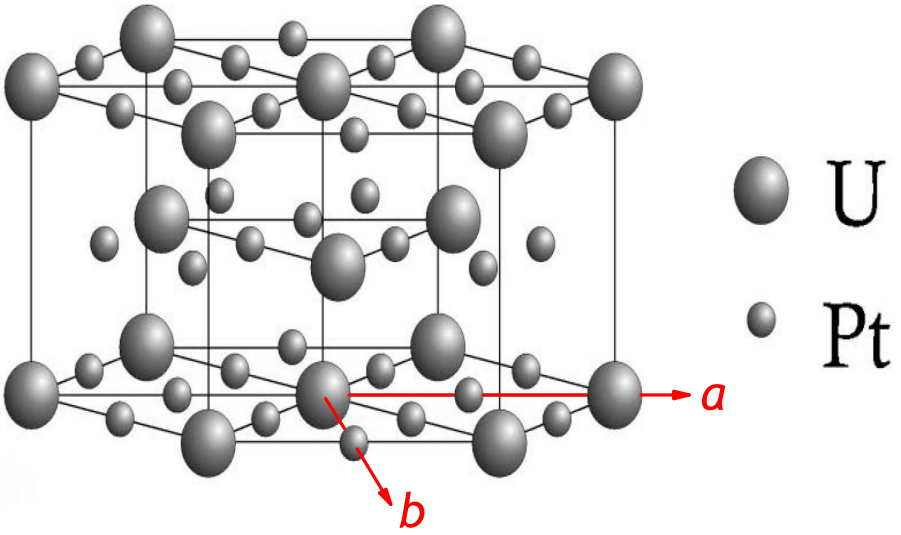

Figure 2.1: A schematic of the crystal structure for UPt_3. The large spheres are the U atoms and the small spheres are the Pt atoms. The arrows indicate the crystal axes. From[7]

the superconducting states. In itself, that makes UPt_3 highly unusual, since magnetism and superconductivity are normally conflicting forms of electronic order.

2.2 Anisotropic Gap Amplitude

Even in the initial papers there were signs that UPt_3 was not a conventional BCS superconductor. The transition temperatures reported varied wildly between different samples, a feature that continued to be true for years until sample quality became consistently high. Studies where non-magnetic impurities were intentionally introduced show a strong dependence on sample purity in the transition temperature[11].

Sensitivity to non-magnetic impurities is a definite sign of an unconventional superconductor. Magnetic impurities suppress superconductivity in

most superconductors by lifting the degeneracy between the electrons in a Cooper pair and scattering them differently, but Anderson stated that scattering off of non-magnetic impurities should not break pairs in a BCS superconductor[12]. Scattering in a system mixes different states and averages the Fermi velocity of the pairs. For an isotropic gap where there is no preferred direction, this averaging does not affect the amplitude. In an anisotropic gap, particularly one with nodes where the gap amplitude goes to zero, scattering changes the amplitude, lifting the nodes and lowering the maxima. In a system where the phase varies and changes sign between different momenta, the averaging can cancel out the gap altogether.

The next significant discovery in UPt_3 came from measurements of the specific heat. In conventional superconductors, as the material passes through the superconducting transition an abrupt peak is observed in the specific heat. This occurs because when the energy gap opens up at the Fermi surface, any excitation has to overcome the magnitude of the gap. This effectively freezes out low-level excitations, meaning that there are fewer excitations capable of transporting heat. In UPt_3, two peaks, separated by approximately 10% of T_C, were observed[13, 14]. This was taken as a clear sign of two distinct superconducting transitions, making UPt_3 the first material with multiple superconducting phases. UPt_3 is still one of very few unambiguous cases of multiple-phase superconductivity, joined only by thorium-doped UBe_{13}[15] and $PrOs_4Sb_{12}$[16]. Some of the initial specific heat data can be seen in Figure 2.2. The transition temperatures have risen with sample quality and are now placed at $T_{C+} = 565mK$ and $T_{C-} = 508mK$.

Additional measurements conducted at high magnetic field revealed a third magnetic phase, in addition to the two low-field phases[17]. A wide variety of transport measurements were performed to further map out the phase di-

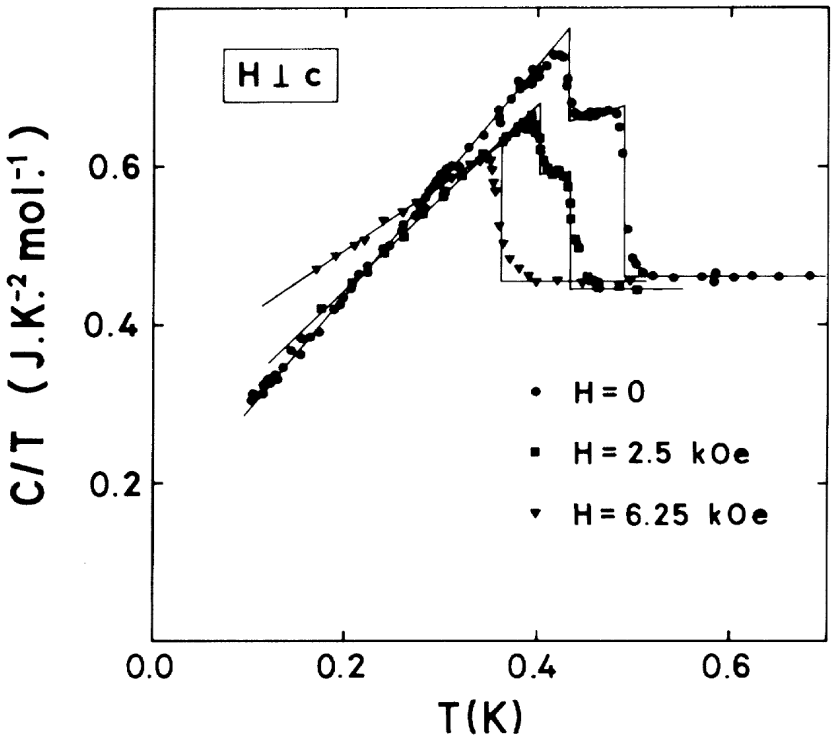

Figure 2.2: Specific heat data for UPt_3 showing the two peaks for the two superconducting transitions. The separation between the two transitions diminishes with applied magnetic field. From[14]

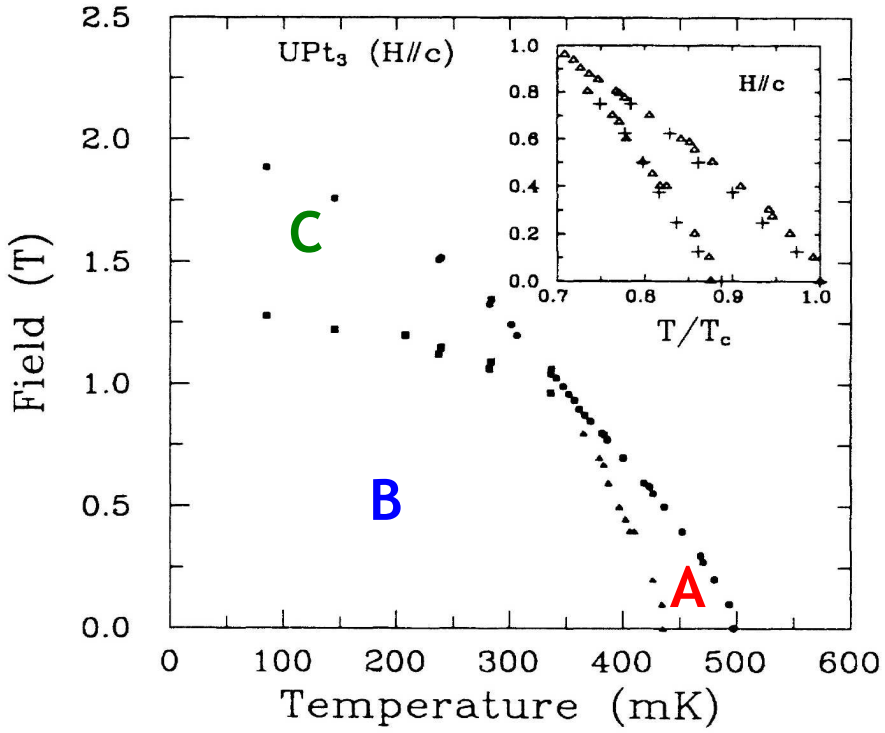

Figure 2.3: Ultrasonic attenuation data mapping out the phase diagram for UPt_3, showing the three different superconducting phases. The transition temperatures have risen slightly over the years as sample quality has increased, and at zero field $T_{c+} = 565mK$ and $T_{c-} = 508mK$. From[17]

agram of UPt_3 and clarify the locations of nodes in the order parameter[18, 19, 20, 21, 22]. These experiments involved directional probes like ultrasonic attenuation and thermal conductivity that tested the mobility of excitations along various crystalline axes. Much like the specific heat measurements, these experiments detected the energy gap by the way it froze out low-energy excitations. In ordinary superconductors, transport properties exhibit an exponential decay as the temperature goes below the superconducting transition. The presence of nodes in the order parameter allow for more carriers, and give linear or low-order power law behavior. Figure 2.3 shows a schematic of the phase diagram for UPt_3.

2.3 Unconventional Symmetry

Along with having an anisotropic energy gap, there were signs from spin-sensitive measurements that UPt_3 had a pairing symmetry that was not the conventional BCS singlet s-wave state. In the BCS model, when dealing with scattering, there are two potential coherence factors affecting the electron matrix elements. Which one is used depends on whether the sign of the matrix element changes under time-reversal. In cases like non-magnetic scattering where the sign does not change, the coherence factor results in the exponential decay described above. In magnetic measurements like nuclear magnetic resonance (NMR), the reverse is true, and a peak in the nuclear spin relaxation rate appears at the superconducting transition[23]. This Hebel-Slichter coherence peak is a hallmark of BCS behavior, but it is absent in UPt_3[24].

Another way that NMR measurements point to unconventional pairing is through measurements of the Knight shift, which is a shift in the resonant frequency that occurs at the superconducting transition. In the BCS model, the Cooper pairs are made of electrons in the anti-symmetric singlet state, such that their spins are opposite to each other. This means that as a material becomes superconducting and the pairs condense out of the Fermi sea, spins that were available to interact with the resonance are effectively gone. This loss of net spin causes the shift in resonant frequency. There is no such shift in UPt_3[24, 25], as shown in Figure 2.4. The lack of any shift means that the spins are still able to interact with the resonance. The main possibility is that the electron pairs have formed a spin-triplet state with symmetric spins, such as in superfluid ^{3}He, though it is also possible that there is a strong spin-orbit scattering term allowing singlet electrons to interact.

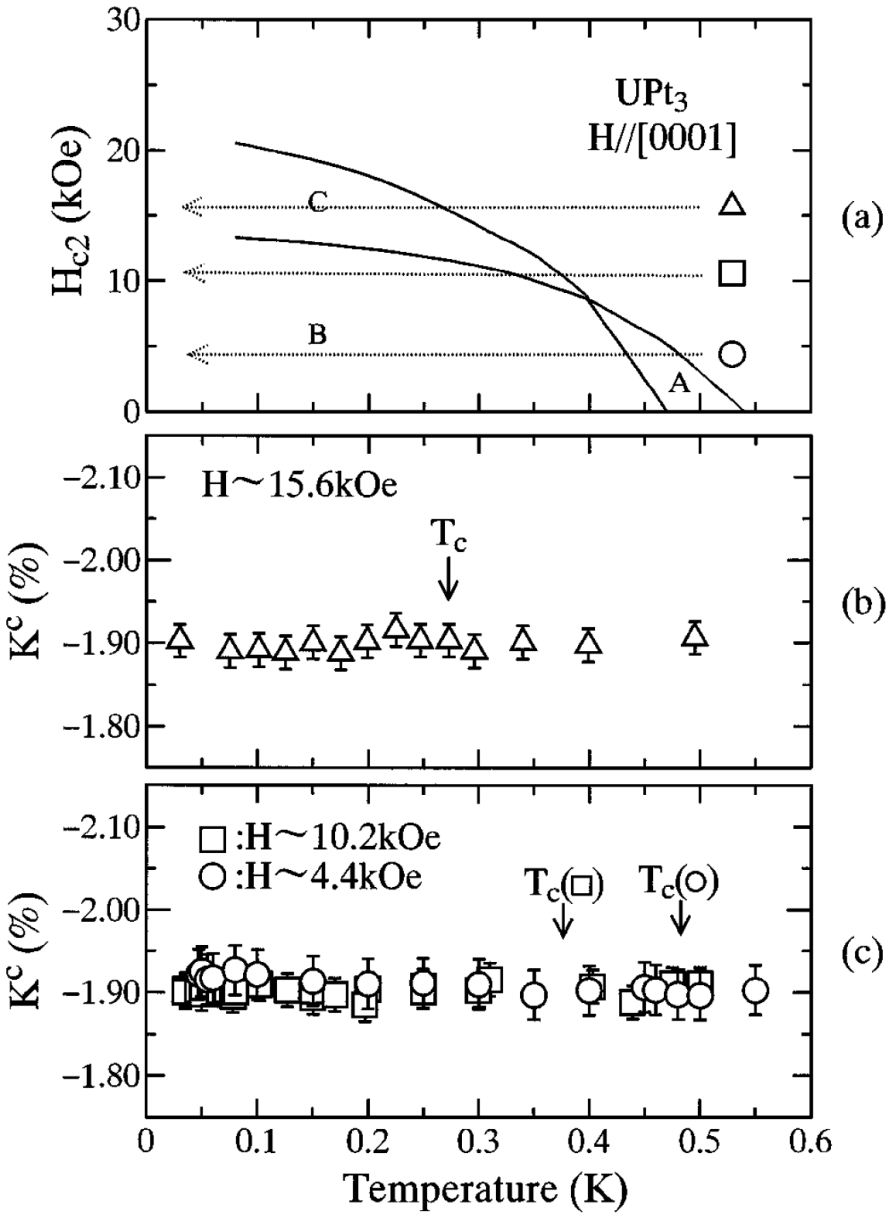

Figure 2.4: NMR data showing the absence of the Knight shift in UPt_3. This points to a spin-triplet pairing symmetry. From[25]

Muon spin resonance (μSR) provides another magnetic probe of the system. In this method, spin-polarized muons are injected into the sample, and the decay time for the polarization is measured. The muons sample a small volume around their location, and in the presence of a magnetic field their relaxation time is increased because they can precess around the magnetic moment. In UPt_3, the relaxation time was observed to increase as the sample passed through the second superconducting transition into the low-temperature B-phase[26]. This increase indicated a spontaneous magnetization of the sample, breaking time-reversal symmetry. This result is somewhat in question because an attempt to reproduce it by a different group was unsuccessful[27]. One of the data plots showing the spontaneous magnetization can be seen in Figure 2.5. If true, this would mean that the superconducting order parameter in the B-phase had a chiral phase, which would induce spontaneous current flow around the circumference of the crystal and create a magnetic moment.

Lastly, it is believed that the antiferromagnetism and superconductivity in UPt_3 are actually linked. A study was performed where neutron diffraction and specific heat measurements were performed simultaneously as pressure was applied[28]. The neutron diffraction could observe the antiferromagnetic order and the peaks in specific heat showed the splitting of the superconducting phases. As the pressure was increased, the antiferromagnetic ordering lessened at the same rate as the splitting of the superconducting phases decreased, and they ultimately vanished at the same pressure. This strong correlation in their behavior was interpreted as a sign that they were correlated in a more fundamental way as well.

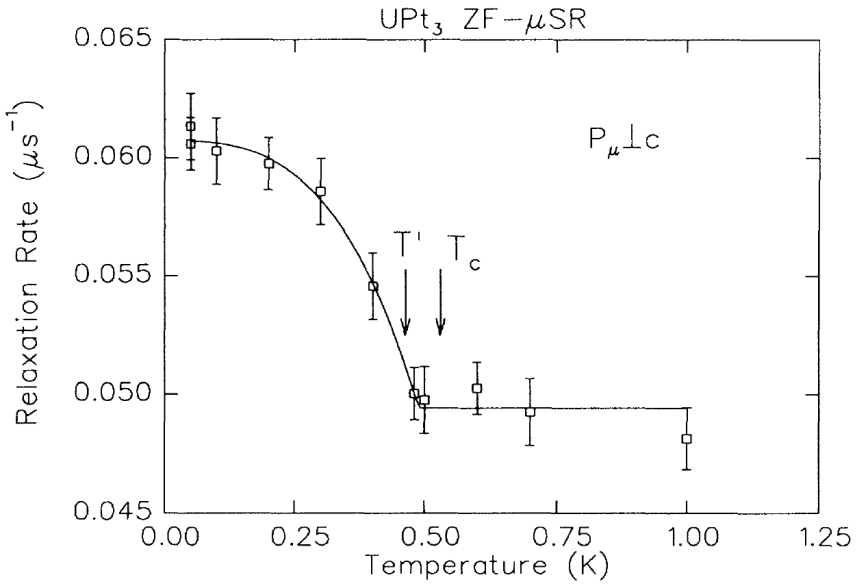

Figure 2.5: μSR data showing onset of spontaneous magnetization in the low-temperature B-phase of UPt_3. This would be an indication of time-reversal symmetry breaking and chiral phase in the superconducting order parameter. From[26]

2.4 Models of the Order Parameter

A great deal of theoretical work has gone into explaining the complicated behavior of the superconducting states in UPt_3. This has resulted in numerous models for the superconducting order parameter, but all of these models were obtained in a relatively similar fashion. The BCS theory does not apply to UPt_3, which is evident in the phase diagram alone. BCS describes a single superconducting state, meaning that at least two of the three superconducting states in UPt_3 must have a different microscopic description. Thus the theoretical work has used a phenomenological approach to describe the superconducting order parameter. An excellent review of the theoretical work done on UPt_3 can be found in [7].

The superconducting state exists within the framework of the crystal lattice, and so the quickest way to narrow down the field of candidate represen-

tations is to study how the Cooper pair wavefunction behaves under operations that leave the crystal structure unchanged. This set of rotations and reflections is known as the point group of the crystal, and the point group for UPt_3 is D_{6h}. Cooper pairs are normally assumed to have zero center-of-mass momentum, and so translations can be neglected. The six representations of the rotation group are A_1, A_2, B_1, B_2, E_1, and E_2. Of these, $A_{1,2}$ and $B_{1,2}$ are one-dimensional representations, and $E_{1,2}$ are two-dimensional representations. When inversion is taken into account, an extra subscript is added depending on whether the representation has uneven ("ungerade") or even ("gerade") parity, giving the representations names like A_{1u}, A_{1g}, etc.

After this initial reduction in the candidate order parameters, further determination is based on evaluating how well predictions based on these representations fit the observed experimental results. Although some early work was done with one-dimensional representations[29, 30], the complexity of UPt_3, in particular the multiple superconducting transitions, has effectively ruled them out in favor of the two-dimensional representations of the order parameter. Of these, the two that best explain the experimental data are the singlet-state E_{1g}[31, 32], and the triplet-state E_{2u}[33, 34]. The equations for the order parameter in each of these representations at zero field can be found in Equations 2.1 and 2.2.

$$E_{1g}\textbf{:} \quad \Delta(k) = \Delta_R(T)k_xk_z + \Delta_I(T)ik_yk_z \tag{2.1}$$

$$E_{2u}\textbf{:} \quad \vec{d}(k) = \Delta_R(T)(k_x^2 - k_y^2)k_z\hat{z} + \Delta_I(T)2ik_xk_yk_z\hat{z} \tag{2.2}$$

In these equations, $\Delta_R(T)$ and $\Delta_I(T)$ represent the magnitudes of the real and imaginary components of the superconducting energy gap, respectively.

The expression for E_{1g} is purely for the magnitude of the superconducting gap because it is a singlet state, but the expression for E_{2u} incorporates the d-vector, which defines the direction of angular momentum for the spin-triplet Cooper pair. Graphical depictions of these representations can be found in Figure 2.6.

Both of these models account for the double superconducting transition by a coupling between superconductivity and the antiferromagnetic moments and feature a real order parameter in the high-temperature A-phase and a complex order parameter in the low-temperature B-phase. Both models feature a variety of line and point nodes that can explain the power-law temperature dependence of transport measurements. There are differences in the predictions made based upon the two different nodal structures, but they are subtle, and comparison with experiment has not been definitive in distinguishing between them. Specifically, both models feature c-axis and basal plane nodes in both the high and low temperature phases, which limits the sensitivity of magnitude probes. The pairing symmetry is a more clear distinction, and the Knight shift measurements point to the triplet E_{2u} case, but UPt_3 has a strong spin-orbit scattering term, and the expected magnitude of the Knight shift is not large. Thus, this one measurement is not conclusive in identifying the correct representation.

The other clear difference between the two models is their degree of phase variation. In each model the phase of the order parameter wavefunction varies in the basal plane as one rotates around the c-axis. In the E_{1g} representation, the phase completes a 2π oscillation in one full rotation. In the E_{2u} representation, the phase completes a 4π oscillation in one full rotation. In the next chapter we will describe an experimental method to test for this difference in phase and distinguish between these two models of the super-

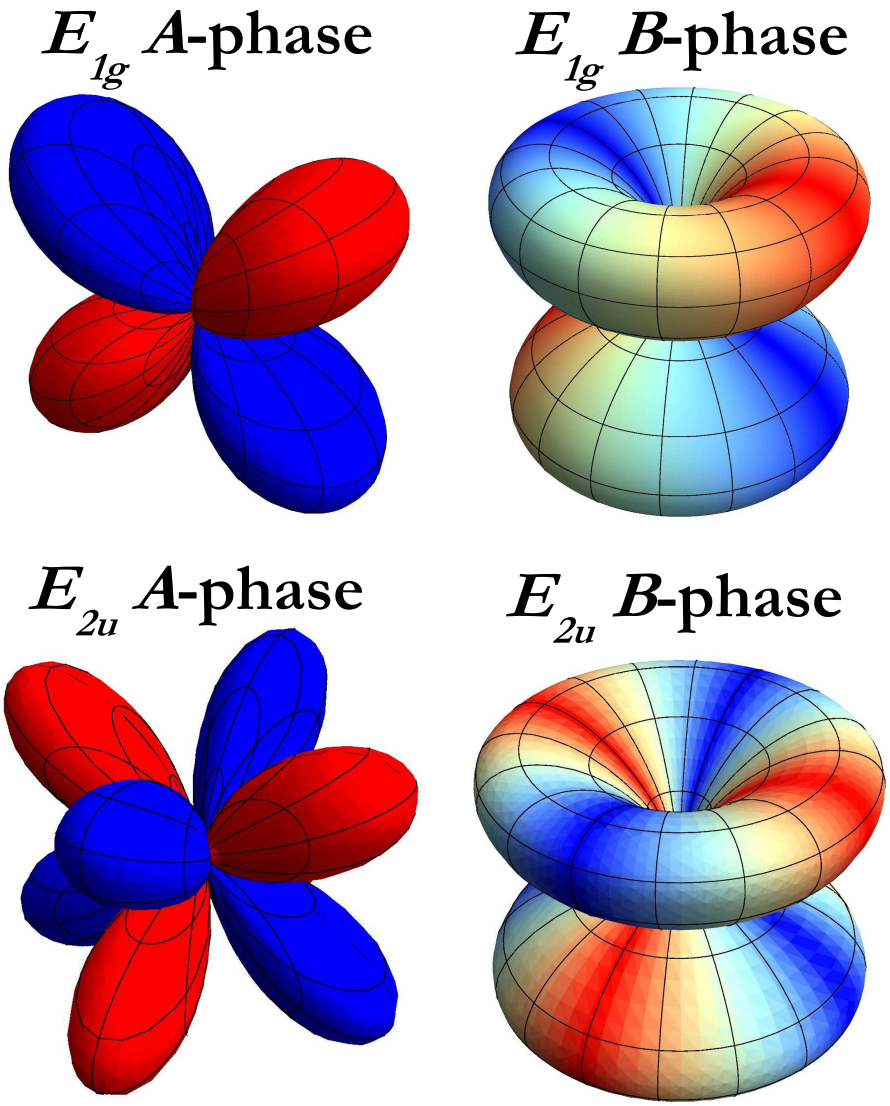

Figure 2.6: Graphical depictions of the E_{1g} and E_{2u} representations of the superconducting order parameter in UPt_3. The A-phase plots are in the region between T_{C+} and T_{C-}. The B-phase plots are in the $T = 0$ limit. The color variation indicates the phase of the order parameter wavefunction, with red indicating the zero phase, and blue indicating a relative phase of π.

conducting order parameter. A correct determination of the superconducting order parameter would tell us a great deal about the interplay between superconductivity and magnetism.

Chapter 3

Josephson Effect and Interferometry

3.1 Introduction to Weak Links

The Josephson effect takes place when two superconductors are brought into close proximity through a weak link. This weak link can take numerous forms, including a thin insulating barrier, a layer of a normal metal, or even a narrow constriction in the superconductor. The key feature of these weak links is that the order parameter wavefunctions of the two superconductors overlap. The order parameter of a superconductor decays exponentially as it enters a neighboring material, but if two superconductors are sufficiently close, these exponential tails can interact, giving a finite probability that Cooper pairs could tunnel from one superconductor to the other. A drawing of this overlapping behavior can be seen in Figure 3.1.

Another important feature of this weak connection between the superconductors is that the phase of one superconductor can be varied independently of other. In fact, if the phase of one superconductor is increased by 2π relative the other, the system returns to its original state, indicating that these weak links are periodic in phase. These weak links are commonly called Josephson junctions, after B. D. Josephson, who predicted their behavior in 1962[35]. We will give an overview of their behavior, particularly as it pertains to our experiment, but there are numerous books that provide more complete theoretical descriptions of Josephson junction devices[36, 37].

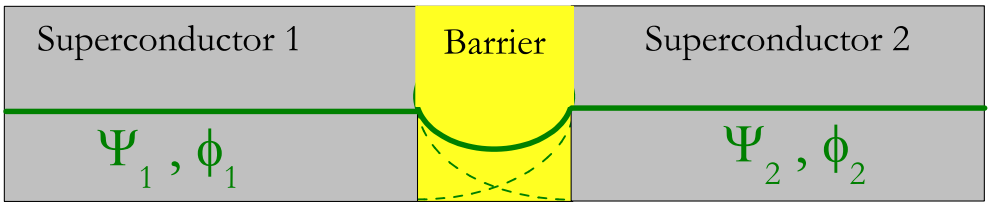

Figure 3.1: Drawing showing how the order parameter wavefunctions of two adjacent superconductors can overlap within a weak link between them.

The prediction that Josephson made was that the supercurrent passing through the junction would be periodic in phase, as given by

$$I_S = I_0 \sin \phi \tag{3.1}$$

where I_S is the current through the junction, I_0 is the maximum supercurrent capable of passing through the junction, and ϕ is the phase difference between the two superconductors. This phase difference is gauge invariant, and so in the presence of an external vector potential, A, must be written as

$$\phi = \phi_1 - \phi_2 - \frac{2e}{\hbar} \int_1^2 \vec{A} \bullet d\vec{l} \tag{3.2}$$

This prediction tells us that a supercurrent will spontaneously flow between two superconductors whenever there is a phase gradient between them; this is known as the d.c. Josephson effect. Josephson also predicted that if a voltage were applied across a junction, it would cause a time-varying phase gradient

$$\hbar \frac{\partial \phi}{\partial t} = 2eV \tag{3.3}$$

This time-varying phase gradient will produce an oscillatory current through

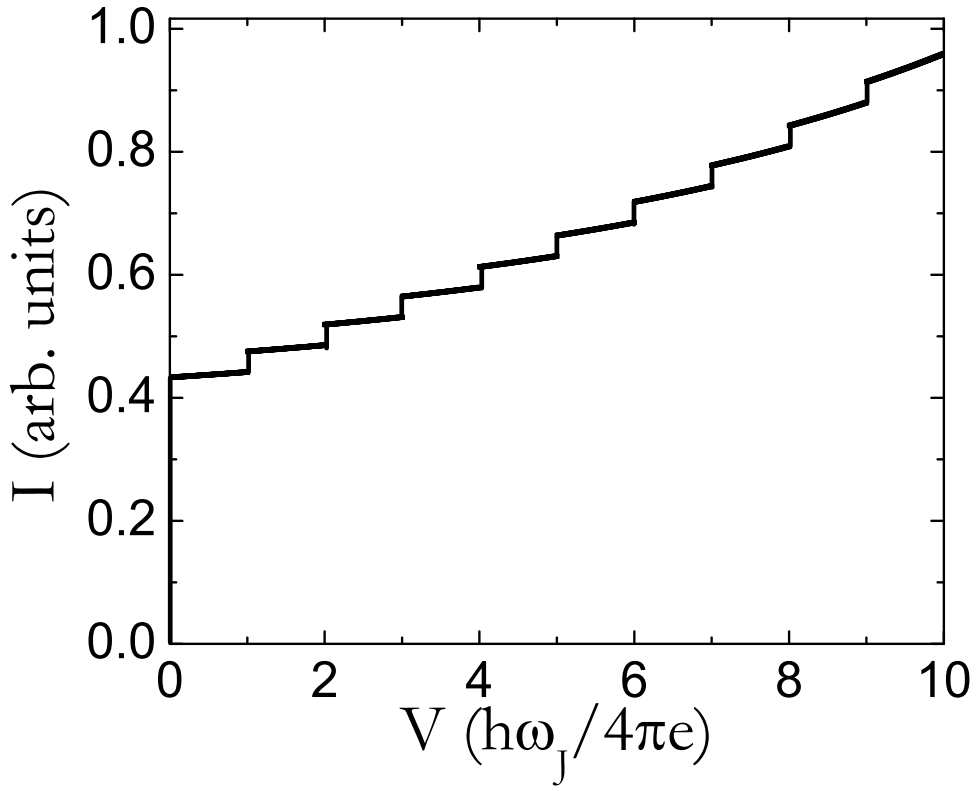

Figure 3.2: Simulation of Shapiro steps in a current-voltage plot for a Josephson junction demonstrating the a.c. Josephson effect. The steps appear at voltage intervals corresponding to the Josephson frequency, ω_J.

the junction, as described by Equation 3.1, which is known as the a.c. Josephson effect. The quantity $2eV/\hbar$ has the units of angular frequency, and is known as the Josephson frequency, ω_J. The corollary to this a.c. response is that if radiation of this frequency is coupled to a Josephson junction it will generate a supercurrent. When these supercurrents are superimposed on a d.c. current plot, they are known as Shapiro steps, and are a characteristic sign of a Josephson junction. A simulation of these steps is shown in Figure 3.2.

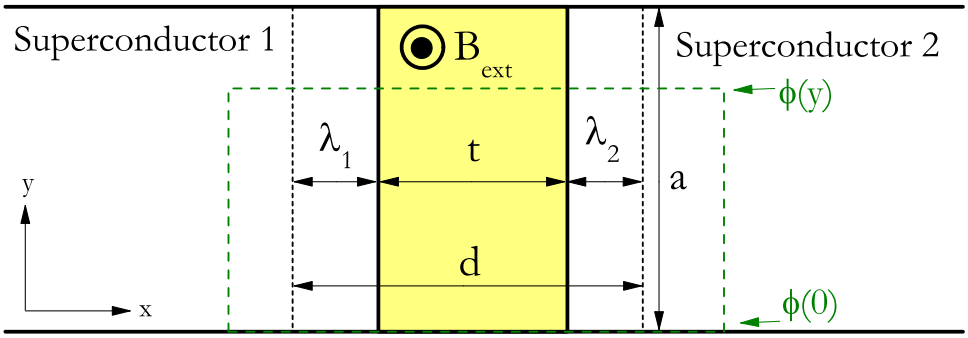

Figure 3.3: Diagram of a Josephson junction in the $y-z$ plane, with a magnetic field, $\overline{B}$, applied along the z-axis. The width of the junction is a, and the thickness penetrated by the magnetic field, d, is equal to the barrier thickness, t, plus the penetration depths of each superconductor, λ_1 and λ_2. The red dashed line indicates the contour of integration for determining the phase difference across the junctions at a given position, $\phi(y)$.

3.2 Josephson Junctions in a Magnetic Field

So far, we have ignored the effect of magnetic fields on the behavior of Josephson junctions, but as shown in Equation 3.2, an external magnetic field will affect the phase gradient between the two superconductors. Let us consider a junction lying in the y-z plane with a magnetic field applied along the z-axis, as depicted in Figure 3.3. Since $\vec{B} = \vec{\nabla} \times \vec{A}$, the line integral of $\vec{A}$ around a contour passing through both superconductors gives the enclosed flux, Φ. The area penetrated by the magnetic field is defined by the thickness of the barrier, t, and the penetration depths of each superconductor, λ_1 and λ_2. If we define one edge of the junction as $y = 0$, then we get an expression for the phase difference across the junction at any point

$$\phi(y) = \phi(0) - \frac{2\pi\Phi(y)}{\Phi_0} = \phi(0) - \frac{2\pi Byd}{\Phi_0} \tag{3.4}$$

where Φ_0 is the flux quantum, equal to $h/2e$ and $d = t + \lambda_1 + \lambda_2$. This means that the phase difference between the superconductors varies across the junction width due to the magnetic field, which also means that the supercurrent across the junction varies across the junction width. In order to find the net supercurrent flow across the junction, we need to integrate the current flow along the width of the junction. For a junction of height c and current carrying capacity J_C, this gives

$$I_C = c \int_0^a J_C \sin \phi(y) dy = I_0 \left| \frac{\sin\left(\pi \Phi_{ext}/\Phi_0\right)}{\pi \Phi_{ext}/\Phi_0} \right| \tag{3.5}$$

This function for the critical current is analogous to a Fraunhofer single slit optical diffraction experiment, and a graph of critical current vs. magnetic flux is shown in Figure 3.4. This relation also assumes that the junction is small enough that the fields produced by the current flowing through the junction are negligible. This is true as long as the junction width is smaller than the Josephson penetration depth, defined as

$$\lambda_J = \left(\frac{\hbar}{2e\mu_0 J_C d} \right)^{\frac{1}{2}} \tag{3.6}$$

This sensitivity to external flux makes Josephson junctions an excellent probe of magnetic field, limited by the size dictated by the Josephson penetration depth. This limitation can be overcome if two Josephson junctions are connected in parallel so that the area between the two paths forms a loop. Since the size of this loop is much larger than the size of the individual junctions, the phase difference across the circuit is dominated by the flux through the loop rather than the flux penetrating the junctions. Assuming the two junctions are equal in size and current-carrying capacity, the supercurrent across the circuit is

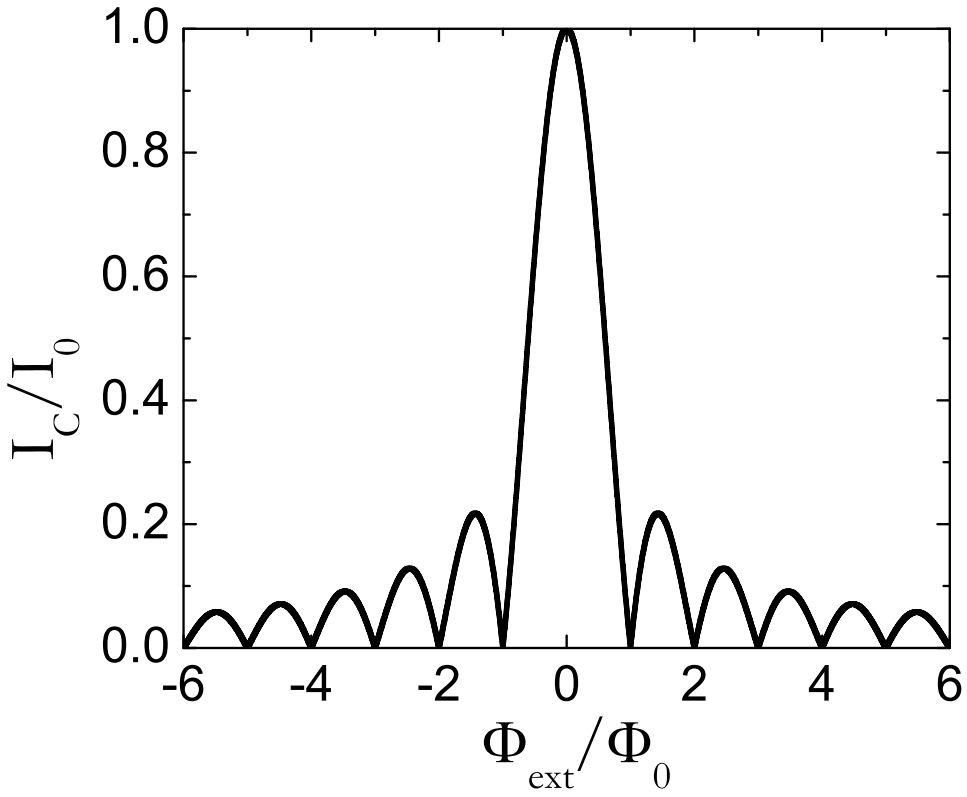

Figure 3.4: Simulation of critical current vs. magnetic flux for a Josephson tunnel junction. Note the analogous behavior to a Fraunhofer single slit optical diffraction pattern.

$$I_c = 2I_0 \left| \cos\left(\pi \frac{\Phi_{ext}}{\Phi_0}\right) \right| \tag{3.7}$$

This type of device is called a Superconducting QUantum Interference Device (SQUID), and is used an extremely sensitive probe of magnetic flux.

3.3 Josephson Effect as a Probe of the Superconducting Order Parameter

The assumption that we have been making in our study of Josephson junctions thus far is that the phase of each superconductor in these devices is a constant. As we have discussed earlier, this is not the case for a wide variety of unconventional superconductors. If the phase of the superconducting order parameter in a material is not isotropic in k-space, it will change the behavior of any Josephson junctions incorporating it. This sensitivity to phase, along with the fact that the tunneling probability across a junction is heavily biased perpendicular to the plane of the junction, means that Josephson junctions are uniquely suited to probe the superconducting order parameter of unconventional superconductors[38].

As an example, consider a SQUID where the two Josephson junctions are fabricated on two different faces of a single crystal of some superconductor, as shown in Figure 3.5(a). Since the tunneling through the junctions is heavily biased in the direction perpendicular to the barrier, each junction is effectively only seeing the phase associated with a single k-space direction. If the superconducting crystal is isotropic in phase, then the SQUID behaves no differently than a conventional SQUID and the critical current is given by Equation 3.7. However, if the order parameter of the superconducting crystal has an intrinsic phase variation such that there is a phase difference

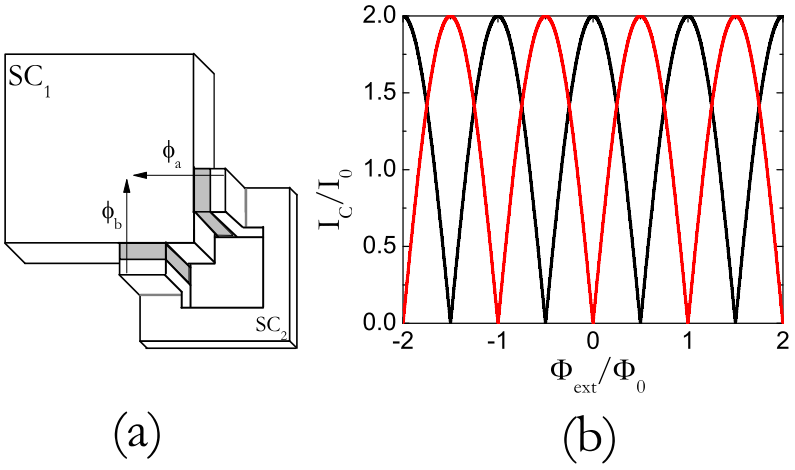

Figure 3.5: (a) A schematic of a SQUID fabricated on the corner of a superconducting single crystal. Each junction is probing a different k-space direction. (b) Simulated plots of critical current through a corner SQUID like that in (a) as a function of external flux. The black curve is for a superconductor with isotropic phase, and the red curve is for a superconductor with an intrinsic phase difference between the two tunneling directions of π.

between the two tunneling directions, the equation is modified to be

$$I_c(\Phi_{ext}) = 2I_0 \left| \cos\left(\pi \frac{\Phi_{ext}}{\Phi_0} + \frac{\delta}{2}\right) \right| \tag{3.8}$$

where δ represents the phase difference between the tunneling directions. Simulated plots of the critical current vs. magnetic flux showing the resulting shift in the pattern are shown in Figure 3.5(b). This technique was first used to provide evidence that the high temperature cuprate superconductors possessed an unconventional d-wave pairing symmetry[39].

The weakness in this experiment is that the $I_C(\Phi)$ plots are periodic and have no well-defined zero. This means that it is hard to distinguish between a shift arising from an internal phase variation in the crystal and a shift due to some external source of magnetic flux penetrating the loop. The answer

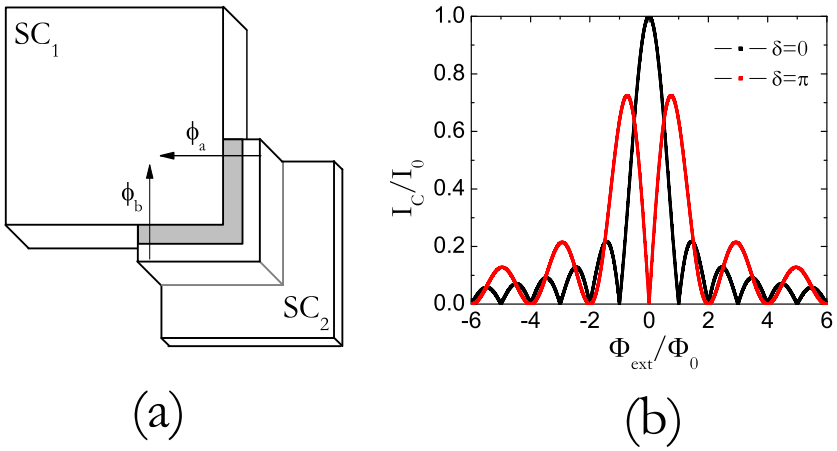

Figure 3.6: (a) A schematic of a Josephson junction fabricated on the corner of a superconducting single crystal so that each half of the junction is probing a different k-space direction. (b) Simulated plots of critical current through a corner junction like that in (a) as a function of external flux. The black curve is for a superconductor with isotropic phase, and the red curve is for a superconductor with an intrinsic phase difference between the two tunneling directions of π.

to this problem is to make a single junction that straddles the corner of the crystal, as shown in Figure 3.6(a). In this case, each half of the junction is probing a different direction of k-space, and the integral in Equation 3.5 has to be broken into two parts:

$$I_C = c\int_0^{\frac{a}{2}} J_C \sin\phi(y)dy + c\int_{\frac{a}{2}}^{a} J_C \sin(\phi(y)+\delta)dy \tag{3.9}$$

In the case where the intrinsic phase difference is π, as it is in the cuprates, this expression can be simplified to

$$I_c(\Phi_{ext}) = I_0\left|\frac{\sin^2(\pi\Phi_{ext}/2\Phi_0)}{(\pi\Phi_{ext}/2\Phi_0)}\right| \tag{3.10}$$

A comparison of the resulting current vs. flux patterns for $\delta = (0,\pi)$ can be seen in Figure 3.6(b). The advantage of this technique over a corner SQUID

is that the patterns have a defined central peak, or envelope of peaks, that mark the zero point of magnetic flux. Even if external fields shift the pattern, the distinctive shape of the patterns allow for identification of the intrinsic phase shift. This technique has been used to confirm the d-wave symmetry of the cuprates[40], and to identify the pairing symmetry in Sr_2RuO_4 as p-wave[41, 42]. We propose to use Josephson interferometry to identify the intrinsic phase variation of the superconducting order parameter in UPt_3.

Chapter 4

Experimental Details

4.1 Crystal Growth

The UPt_3 crystals that we use were grown at Northwestern University by W. P. Halperin's research group[43]. They were grown in an electron beam floating zone furnace in ultra-high vacuum. In this technique, a stoichiometric ratio of uranium and platinum powders were pressed into a cylinder, which was then arc-melted into a polycrystalline rod. This rod was then placed into the furnace, where it was passed slowly (over many hours) through the focal point of the electron beam. This process was repeated several times, until the lowest energy configuration was reached, producing a single-crystalline rod. A picture of one of these rods can be seen in Figure 4.1.

After coming out of the furnace, the crystal axes were identified by x-ray diffraction, wafers were cut out of the rod by electro-discharge machining, and reference flats were cut for the a- and b-axes. In our case, the c-axis of the crystal was nearly parallel with the rod, and was thus perpendicular to the plane of the wafers we used. These wafers were then annealed at 850°C for 7 days (14 days including ramping up to temperature and back down) in ultra-high vacuum to release stress and disorder in the crystal lattice. The residual resistivity ratio (RRR) of a material, given by the ratio of resistance at room temperature to just above the superconducting transition, is often used as a measure of crystal purity because the resistance ratio depends directly

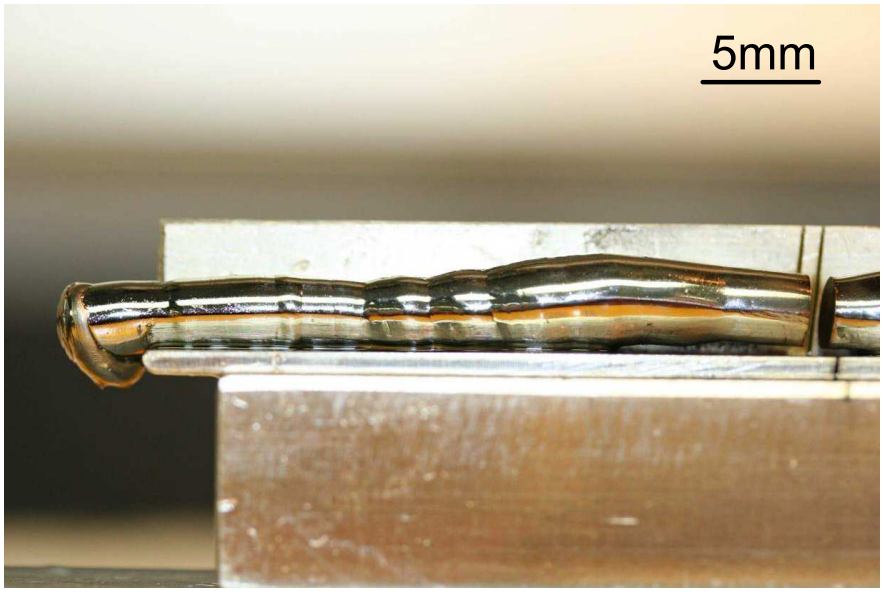

Figure 4.1: A photograph of a single-crystalline rod of UPt_3 after coming out of the electron beam floating zone furnace. A wafer has already been cut from the rod.

on the mean free path of scattering sites and thus impurity concentration. After annealing, the RRR of our crystals ranged from 900 to 1100, compared with typical values in the literature of ≈ 500[44, 25, 45], which indicates the exceptional purity of the samples.

4.2 Sample Fabrication

In order to make useful Josephson junctions on the crystals, a flat surface perpendicular to the desired tunneling direction had to be found or made. As-grown or cleaved surfaces are ideal for this purpose due to their smoothness and because the lattice at the surface is undamaged. We made use of the as-grown surfaces of our wafers for the angular dependence measurements discussed in Section 6, but Josephson interferometry requires corners that the as-grown wafers do not provide. Unfortunately UPt_3 does not cleave

well, and so we had to polish the surfaces we wanted. We used Crystalbond® to mount the crystals onto a micrometer polishing stage. The surfaces were then polished with a variety of diamond lapping films, concluding with a $0.3\mu m$ film.

After preparing the surfaces, the crystals were glued to a glass substrate in preparation for masking. We cut our substrates out of frosted glass slides, because it provided better adhesion for the glue. The substrate was covered with a very thin layer of Pyralin® polyimide coating, normally used as a photoresist rather than as a glue, that proved compatible with large thermal cycles, high vacuum conditions, and good metal film growth. The polyimide was baked at 60°C for 20 minutes until it was tacky, and then the crystal was placed on the substrate. The polyimide wicked partly up the side of the crystal, providing a smooth interface. Then the polyimide was baked at 140°C for 30 minutes until it was fully cured.

The junctions and leads were defined using small strips of Riston® dry photoresist placed by hand with tweezers under a microscope. Junctions sizes of 50x100μm can be achieved with this method. After masking, the samples were placed in vacuum, the surfaces were ion milled briefly to remove organic impurities, and metals were deposited onto the surface via thermal evaporation. The sample stage was rotated during evaporation to allow the films to coat both the crystal face as well as the surface of the substrate. $150nm$ of Cu was deposited as the normal metal barrier for the junctions, and $800nm$ of Pb was used as the superconducting counter-electrode. The effective thickness of the junctions was $\approx 1\mu m$, after including the superconducting penetration depths. Pictures of the surface of our samples after masking and after evaporation can be seen in Figure 4.2. A picture of an entire sample is shown in Figure 4.3.

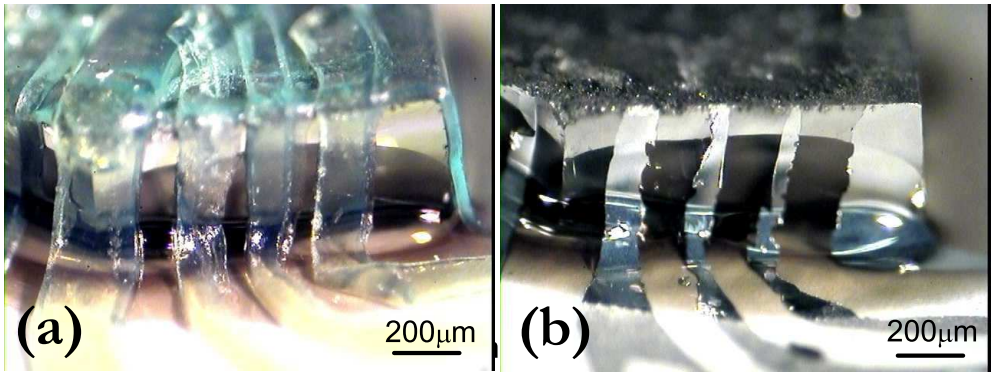

Figure 4.2: (a)A photograph of one of our samples after being masked with Riston®. (b)A photograph of one of our samples after evaporation of the metal films and removal of the mask.

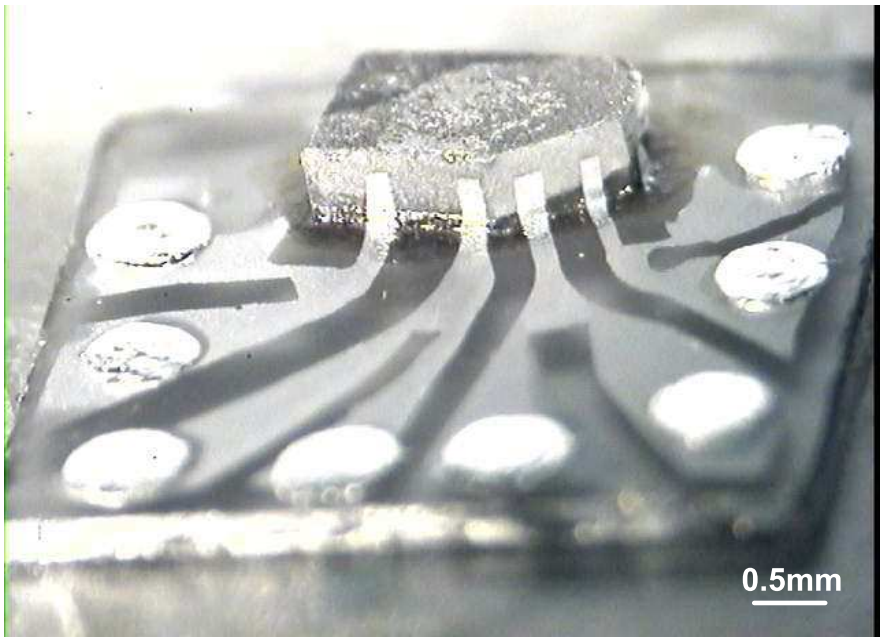

Figure 4.3: A photograph of one of our samples - the crystal is the large block in the upper middle with four edge junctions evaporated on its surface. The lines of Pb film and indium pads are also visible.

4.3 Measurement Setup

4.3.1 Cryogenics

In order to attain the low temperatures necessary to fully probe the different superconducting phases of UPt_3, we used a $^3He/^4He$ dilution refrigerator. A dilution refrigerator achieves its cooling power through essentially the same evaporative mechanism as standard refrigerators, but instead of moving atoms across the liquid/gas phase boundary, it moves ^3He atoms in solution with ^4He from a rich concentration phase to a dilute phase. These two phases spontaneously develop when a mixture of ^3He and ^4He is cooled below $\approx 850mK$.

Achieving the lowest temperatures requires circulating the ^3He in the system continuously. This process is initiated by heating the dilute phase in a still outside the mixing chamber and pumping on the vapor. Because the vapor pressure of ^3He is several orders of magnitude higher than ^4He below 1K, it is preferentially removed from the dilute phase. This causes ^3He from the rich phase to cross over the phase boundary to maintain a constant concentration, taking heat with it. The ^3He that is removed is returned to the system by condensing it through a 1K pot, which is cooled via evaporating ^4He from the bath, and then passed through a series of heat exchangers to take advantage of the cold gas leaving the system.

Our particular dilution refrigerator was a Kelvinox TLM® (Top Loading into Mixture). It differs from other dilution refrigerators in that the sample stage is lowered directly into the mixing chamber, providing direct contact between the sample and the mixture. It also allows for rapid sample changes because the mixture can be left in the refrigerator while the sample probe is removed and modified. It has a cooling power of $250\mu W$ at 100mK. Its base

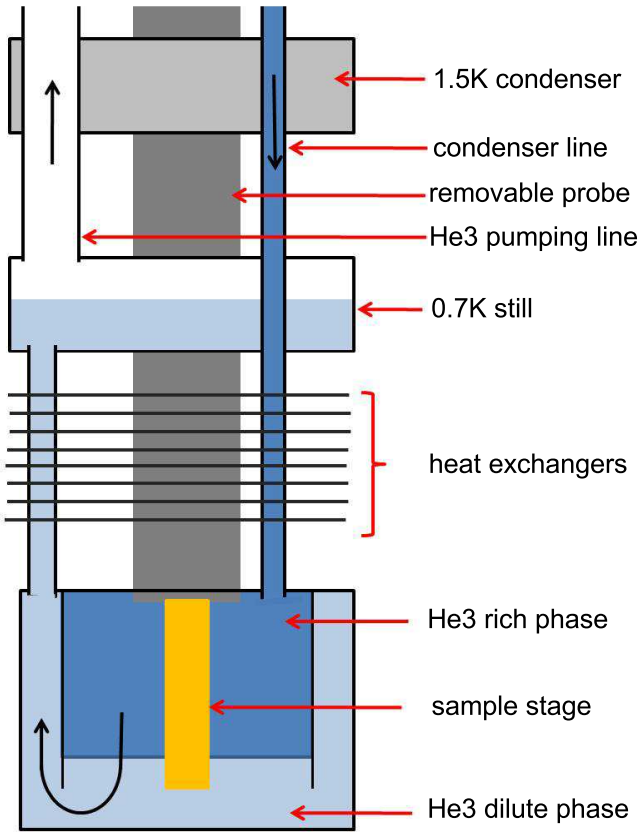

Figure 4.4: A diagram of our dilution refrigerator setup.

temperature is below 10mK, but that range was not relevant to us because UPt_3 maintains an internal temperature of $\approx 100mK$ through radioactive self-heating[46]. We observed this self-heating as a flat plateau in plots of the critical current vs. temperature in our junctions. A schematic of our dilution refrigerator can be seen in Figure 4.4. The temperature can be controlled by varying the heat applied to the mixing chamber, and is stable to within $\pm 1mK$ between 10mK and 700mK. Above 700mK, the temperature is stable within $\pm 3mK$.

Previous experiments on UPt_3 have had difficulties with magnetic flux trapping in the system[45], and so rather than use the large superconducting magnet built into the refrigerator dewar, we made our own magnet that could be placed inside magnetic shielding. We built a small superconducting solenoid that fit around the sample stage, and then surrounded the sample stage and solenoid with Cryoperm® and lead cans to provide the necessary magnetic shielding ($H_{residual} \approx 10^{-4}G$). The refrigerator itself is located in a metal screen room to keep out radio frequencies, and is mounted on an air-floated table to reduce vibrations (pumps are located in a separate room).

4.3.2 Electronics

The principle measurements for this experiment were taking current vs voltage curves to extract the critical currents of the junctions, and tracking the change in critical current as a magnetic field is applied. The primary difficulty in taking these data was finding a setup with the sensitivity to record the extremely small signals. The normal state resistance of our junctions was usually $\approx 10n\Omega$, which when combined with critical currents of $\approx 100\mu A$ gave us a signal of $\approx 1pV$. Ordinary preamplifiers would not give us enough

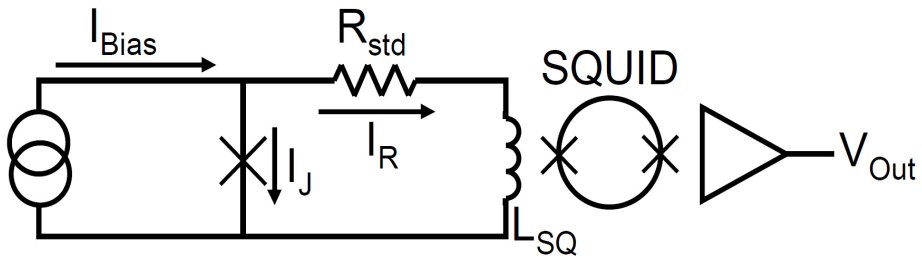

Figure 4.5: A diagram of the SQUID potentiometer circuit. When the junction enters the normal state, the current divides between the junction and the standard resistor, generating a signal in the SQUID.

signal, and so we inductively coupled our circuit to a SQUID to take advantage of their exceptional flux sensitivity. A schematic of the circuit is shown in Figure 4.5.

In this setup, the junction is placed in parallel with a known resistor and a small coil, which is inductively coupled to a commercial dc SQUID made by Quantum Design. It is important to note that all the wires on this parallel path, except for the standard resistor, are superconducting. As long as the junction is in the superconducting state, all of the current applied will pass through the junction, and no magnetic flux will be generated through the SQUID. As soon as the applied current (I_{Bias}) exceeds the critical current of the junction, causing it to enter the normal state, the current will divide between the two paths proportional to their resistances. The current passing through the standard resistor (I_R) and the coil (L_S) will generate flux that is picked up by the SQUID and read out as a voltage.

The SQUID amplifier we used outputs $0.73V$ per Φ_0 of flux in the SQUID, and the inductive coil creates $1\Phi_0$ of flux per $195nA$ of current passing through it. As can be seen in the diagram, the voltages across the junction and the standard resistor are equal (induced voltage from the inductor

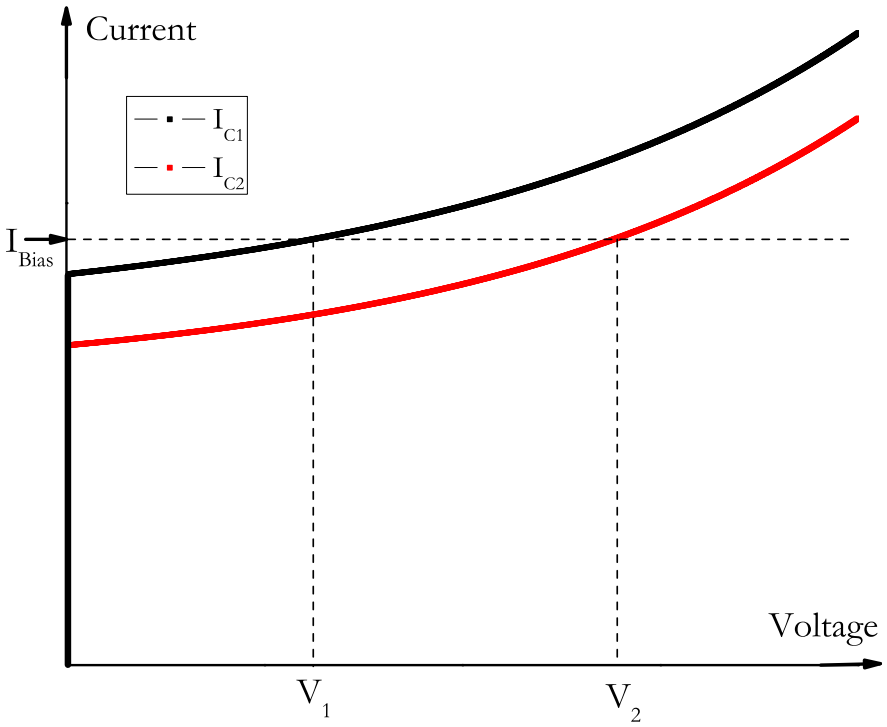

Figure 4.6: An illustration of how we track the critical current in a junction. For a given bias current, the output voltage changes proportionally with the change in critical current.

is negligible because both L_S and dI/dT are very small), and so we find for a typical standard resistance of $10\mu\Omega$:

$$V_J = I_R * R_{std} = V_{out}\left(\frac{195nA}{\Phi_0}\right)\left(\frac{\Phi_0}{0.73V}\right) * 10\mu\Omega = 2.67 \times 10^{-12} V_{out} \quad (4.1)$$

The choice of the standard resistance value is an important one, since the SQUID has a finite range that depends on the normal state resistance of the junction and the amount of current applied to the system. Also, the voltage resolution of the SQUID potentiometer is limited by the Johnson noise in the standard resistor, which is the equivalent of several nA. In our case, we made our standard resistor out of a small length of 40AWG copper wire soldered in series with the superconducting wires.

In order to take the diffraction patterns, it was necessary to track the critical current continuously as the magnetic field was swept. The simplest way to do this is to bias the junction into the normal state, and leave it at a constant current value, and then record the voltage as we sweep the magnetic field. The voltage in this case is proportional to the critical current value, as seen in Figure 4.6, and gives us a qualitative diffraction pattern. This method was used quite often in quickly characterizing a junction and finding the appropriate ranges for the field. A slightly more involved method uses a feedback method to track the critical current directly. A computer program is used to monitor the output voltage and changes the bias current to maintain the voltage at a given setpoint. The setpoint is chosen to be as small as possible, usually just beyond the noise level. In this way, as soon as the junction transitions, the setpoint is reached, and the current is maintained within ϵ of the critical current value. Meanwhile, a separate program monitors the bias current value and sweeps the magnetic field.

Beyond the SQUID electronics mentioned above, we used two current supplies, one each for biasing the junction and providing current to the magnet, a computer to run the Labview control programs, and a digital to analog converter to mediate between them. We found it important to use battery-powered dc current supplies to reduce the current noise introduced to the system. Also, because the standard resistor was so small and the SQUID was so sensitive to any current passing through the input coil, we were very susceptible to picking up an induced electro-motive force from any exposed area between the wires going to the SQUID. We had to sweep the magnetic field very slowly ($\approx 100mG/minute$) and wrap lead foil around every exposed wire for shielding. Even an area of $0.5mm^2$ will intercept enough magnetic flux to drive $\approx 4\mu A$ though the SQUID input coil.

Chapter 5

Phase-Sensitive Measurements in UPt_3 with Josephson Interferometry

In this chapter, I present the results of critical current modulation with applied magnetic field in UPt_3-Cu-Pb Josephson junctions. I measured eleven edge junctions, three corner junctions, and a single corner SQUID. Each of these junctions was measured during numerous separate thermal cycles. All the measurements reported in this chapter were taken well below the second superconducting transition in the low-temperature B-phase. The data in this chapter have been reported in [47].

5.1 Junction Characterization

Before attempting to observe intrinsic phase differences or complex order in UPt_3 with corner junctions, we first spent some time optimizing edge junctions and characterizing their behavior, in order to develop a well understood starting point. The junctions exhibited nearly ideal resistively-shunted junction (RSJ) behavior, as shown in Figure 5.1(a). As mentioned previously, the normal state resistances of the junctions were very small, yielding voltages in the picovolt range.

We applied an ac modulation to the junctions as a further test of their behavior, and measured Shapiro steps, confirming their Josephson character. Due to the low voltage scales ($\approx pV$), the Shapiro steps are indeed at much lower frequencies than the microwave frequencies normally used, in accor-

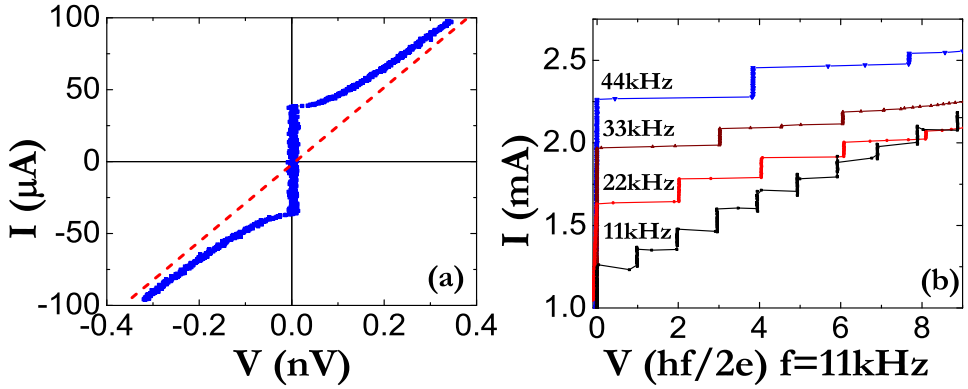

Figure 5.1: (a)A characteristic IV plot for a junction, showing classic RSJ behavior. (b)Shapiro steps from a junction, confirming Josephson behavior.

dance with the Josephson relation ($0.5GHz/\mu V$). Several of these Shapiro steps plots are displayed in Figure 5.1(b).

We also took diffraction pattern measurements on these edge junctions. Though not perfect, the patterns were in nearly all cases approximately Fraunhofer in form, indicating a nearly uniform phase across the junction. They were also symmetric around zero applied field, which shows that there was negligible residual background field, and they were symmetric when biased to negative current instead of positive, confirming they are in the small junction limit where fields generated by the tunneling current can be neglected. An important point to note for the corner junction data presented later is that all of these features indicate a junction that is free of trapped Abrikosov vortices, showing that our fabrication and shielding measures were effective. One of the diffraction patterns from our edge junctions is shown in Figure 5.2.

It is worth mentioning that even though the B-phase of UPt_3 is expected to be chiral and exhibit TRSB, similar to Sr_2RuO_4, we saw no evidence for chiral domains in UPt_3, such as hysteresis or switching noise in the diffraction pat-

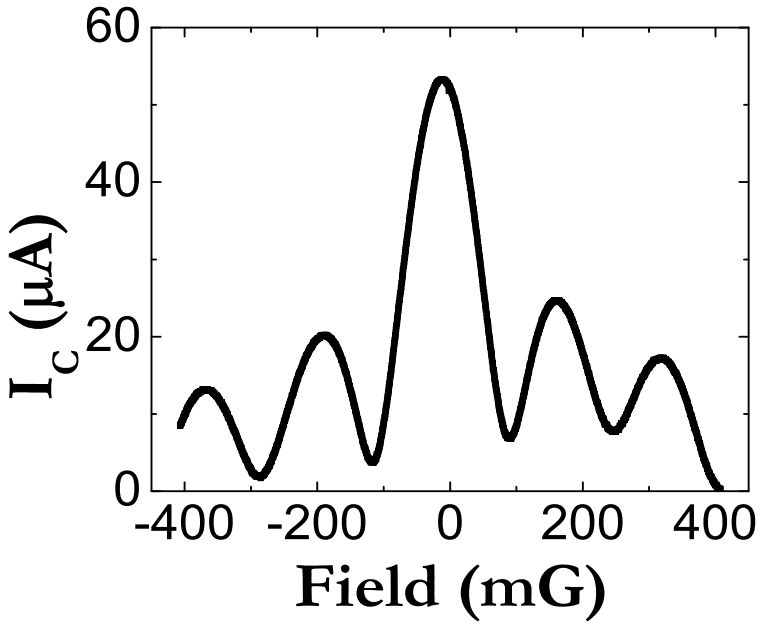

Figure 5.2: A characteristic diffraction pattern plot for one of our edge junctions. The shape is approximately Fraunhofer and symmetric around zero field, indicating uniform phase and no vortices.

terns. Previous work on Sr_2RuO_4 edge junctions consistently demonstrated dynamic behavior with changing magnetic fields or time, indicating that the complex superconducting order parameter formed domains with phase winding in opposite directions[41]. The complete absence of this behavior in UPt_3 points to a superconducting order parameter that is uniform throughout the entire crystal.

5.2 Corner Junctions

After establishing the behavior of our junctions when probing only a single k-space direction, we measured junctions fabricated so that they straddled the corner between the *a*- and *b*-axes. In this configuration the junction is probing two k-space directions simultaneously, and if those two directions have different relative phases the interference between them will show up in

the diffraction pattern. We hoped to be able to distinguish between the two leading theories for the superconducting order parameter, which each predict a different periodicity of phase variation in the basal plane. A rotation of 90° about the c-axis causes a phase shift of $\pi/2$ in the E_{1g} model, but a phase shift of π in the E_{2u} model. Figure 5.3 shows simulations of the predicted diffraction patterns that should be observed for each of the models in the low temperature phase.

These corner junctions behaved quite differently than the edge junctions, even when compared to edge junctions made in the same fabrication cycle. In all cases the diffraction patterns they produced exhibited features that were asymmetric with respect to field polarity. The asymmetry was not caused by the self-field effect of the bias current passing through the junction, because the pattern was symmetric with respect to the direction of bias current flow. Asymmetry with respect to field polarity shows that the system has a preferred magnetic direction, and is a characteristic sign of a complex order parameter symmetry and TRSB.

Despite the irregular shape of the patterns, they were very stable and reproducible. There were still no signs of dynamics with changing field or time, ruling out mobile domains. Raising or lowering the temperature (without exceeding the superconducting transition) decreased or increased the magnitude of the critical current, as expected, but left the shape of the patterns unchanged. The only thing that changed the diffraction patterns in the corner junctions was a complete thermal cycle that took the system out of the superconducting state and cooled it back down, after which it would have a new, but also reproducible and consistent, pattern.

After numerous thermal cycles and diffraction pattern measurements on the corner junctions, we noticed that the patterns could be grouped into

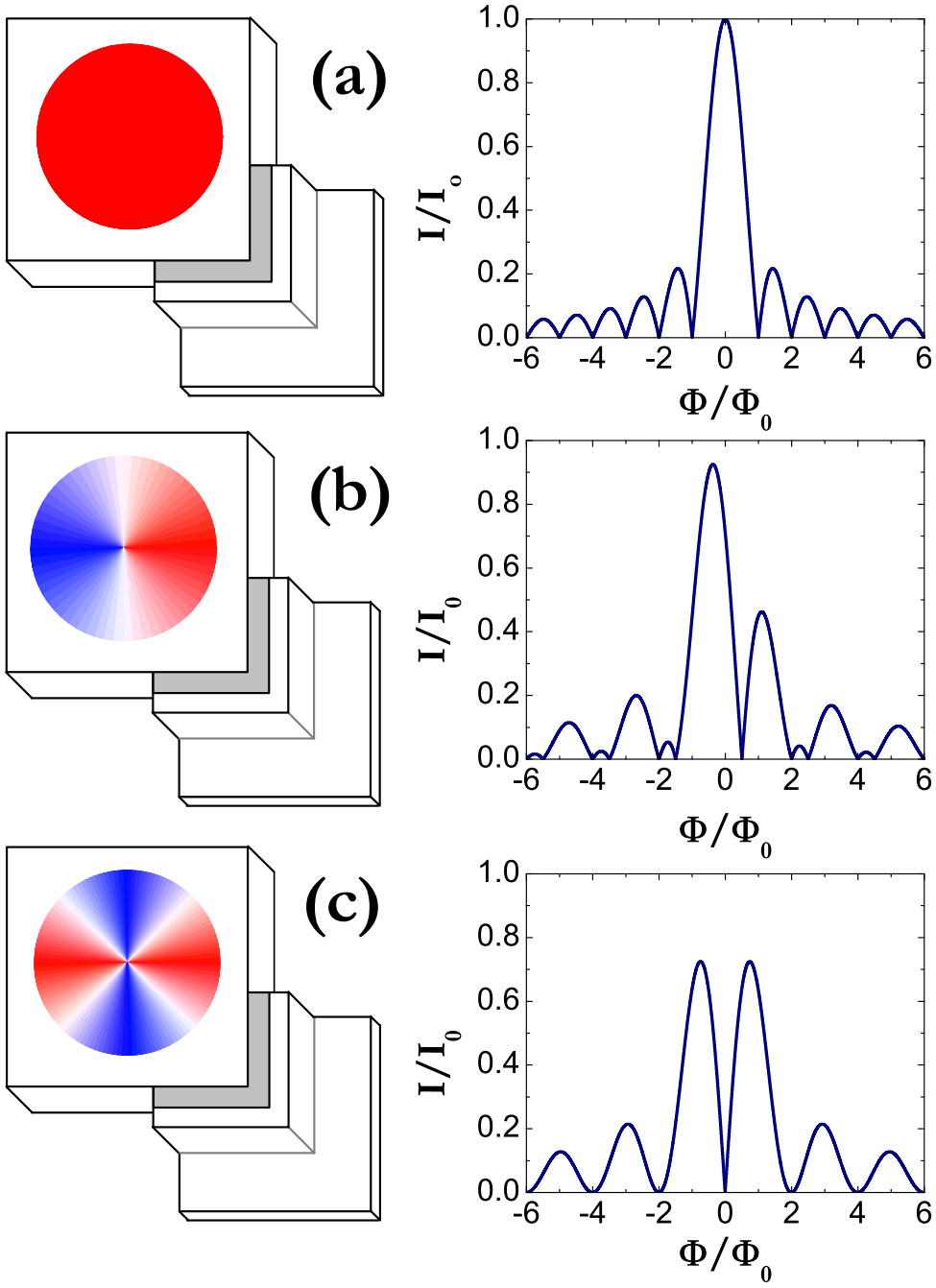

Figure 5.3: Planar representations of the order parameter laid on top of a schematic of a corner junction, with the corresponding diffraction pattern placed alongside. (a)An s-wave order parameter produces the classic Fraunhofer pattern. (b)The E_{1g} B-phase produces an asymmetric double peak. (c)The E_{2u} B-phase produces a symmetric double peak.

three or four qualitatively similar patterns. The main feature we looked at in making these groupings were the number of strong peaks in the pattern.

Any attempt to explain these complicated patterns has to account for the changes in patterns with thermal cycling, which requires some dynamic mechanism. The most obvious candidate is vortices being trapped near the junctions. In the edge junction measurements, we could consistently get vortex-free diffraction patterns, indicating that our magnetic shielding and slow cooling cycles were sufficient to prevent flux-trapping in the bulk of the junctions. The surface treatments for the corner junctions are identical to the edge junctions, and so there is no reason to expect vortices to be more likely to enter the junction, with the possible exception at the corner itself.

Even well-polished surfaces are prone to chipping at the edge, and while our edge junctions are usually masked so that the junction is entirely within the polished surface, the very definition of a corner junction means that it contains the shared edge of two polished surfaces. Though the corners appear optically smooth, some degree of faceting at the region where two surfaces meet is probable. Surface damage can easily suppress superconductivity in an unconventional superconductor and it is possible that our corners are providing a pinning site for vortices or a nucleation site for vortex entry. We did send one sample back to Northwestern for re-annealing after polishing, in an attempt to remove any disorder we introduced. The result was increased magnitude of the critical current, but no change to the shape of the diffraction patterns.

With the possibility of vortices in mind, we have tried modeling corner junctions that combine an intrinsic phase shift with a vortex trapped near the corner. We tested phase shifts corresponding to three candidate symmetries: 0 (s-wave), $\pi/2$ (E_{1g}), and π (E_{2u}). We modeled a vortex as a

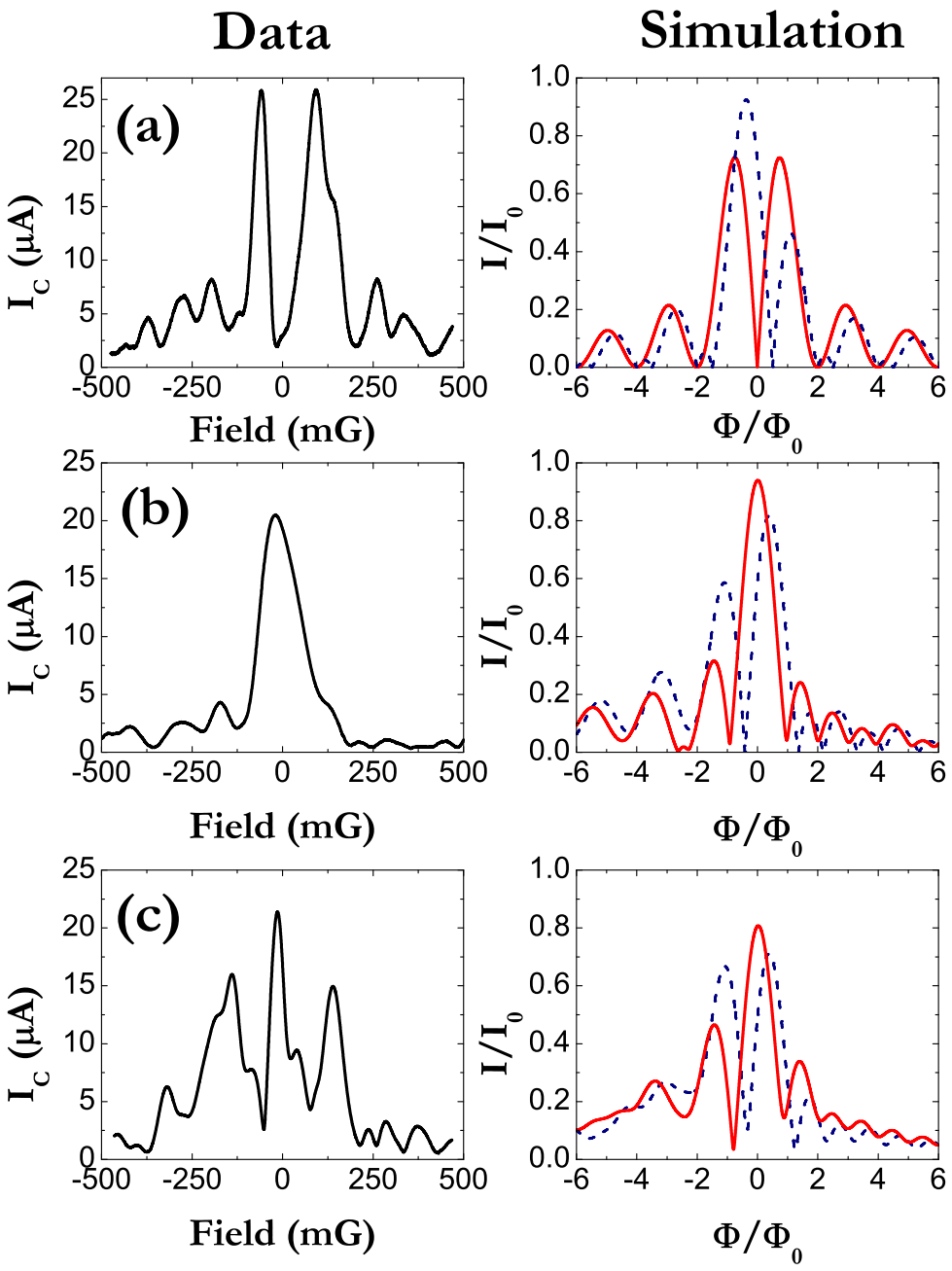

Figure 5.4: Comparisons of corner junction diffraction patterns (T=60mK) with simulations. The three data plots are representative of the three recurring patterns we observed. The simulations assume a single vortex located at the corner of the junction, with the location of the corner allowed to vary by 10% of junction width. Simulations with solid lines assume the E_{2u} representation, and simulations with dashed lines assume the E_{1g} representation.

Gaussian contribution to the flux through the junction with integrated flux = $\Phi_0/2$ and width equal to 3% of the junction width. The junctions are not perfectly symmetric around the corner, and so we allowed the location of the corner (and thus the vortex) to vary by 10% of the junction width. We compared the resulting patterns with our data, and comparisons of representative diffraction patterns to the simulations that best matched them are given in Figure 5.4.

We did not attempt to model the junctions exactly, but focused on matching the number and relative size of the central peaks in the diffraction patterns. Throughout the series of cooldowns, patterns like that in Figure 5.4(a) occurred the majority of the time, suggesting that it is the vortex free state. It also matches well with a phase shift of π with no vortex. Though qualitative, we found this comparison supported the E_{2u} representation more strongly than the E_{1g} representation.

5.3 Corner SQUID

In an effort to avoid any complications caused by the material properties of the corners, we fabricated two junctions, one on either side of the corner, forming a dc SQUID with a loop area of $300\mu m^2$, which is much larger than the magnetic area of the individual junctions ($\approx 25\mu m^2$). Each junction was located in a clean part of the surface away from any edge effects, and any vortex trapped within the corner of the crystal would be screened from the SQUID loop by the Meissner effect. In this arrangement, an intrinsic phase difference in the crystal would show up as a shift in the peak of the critical current modulation, as given by:

$$I_c(\Phi_{ext}) = 2I_0 \left| \cos\left(\pi \frac{\Phi_{ext}}{\Phi_0} + \frac{\delta}{2}\right) \right| \tag{5.1}$$

Unlike a single junction, the periodic modulation of a SQUID does not provide a central peak to reveal the zero point of magnetic flux, so extra care is required to rule out extrinsic shifts in the pattern. The two main sources of extrinsic flux are fields from the bias current through the junctions and residual background field that was not adequately screened. In the first case, if the two junctions are not identical, the current will divide unevenly between them. This unequal current flow between the branches of the loop will couple field into the SQUID, shifting the pattern. To account for this, we biased the SQUID at various current levels as shown in Figure 5.5(a), and noted the location of the peaks at each current value. As long as the bias current level is not changed too much, it is simple to match each peak and track the shift in its location. After several iterations, a correlation between the current level and the induced flux can be obtained, and the peak location can be extrapolated to zero bias current[39].

The amount of residual external field or trapped flux in the SQUID loop should be different with every cooldown, and so the best way to account for residual external field or trapped flux is to repeat the measurement numerous times and average the results. We performed seven thermal cycles, with the results plotted in Figure 5.5(b). The results cluster around $\Phi_0/2$, corresponding to a phase shift of π, which agrees with our corner junction results and also supports the E_{2u} model.

One complication is that the slope of the extrapolations is not a constant. For a given pair of junctions, the asymmetry should not change with time, and the flux introduced by the uneven current flow should remain the same.

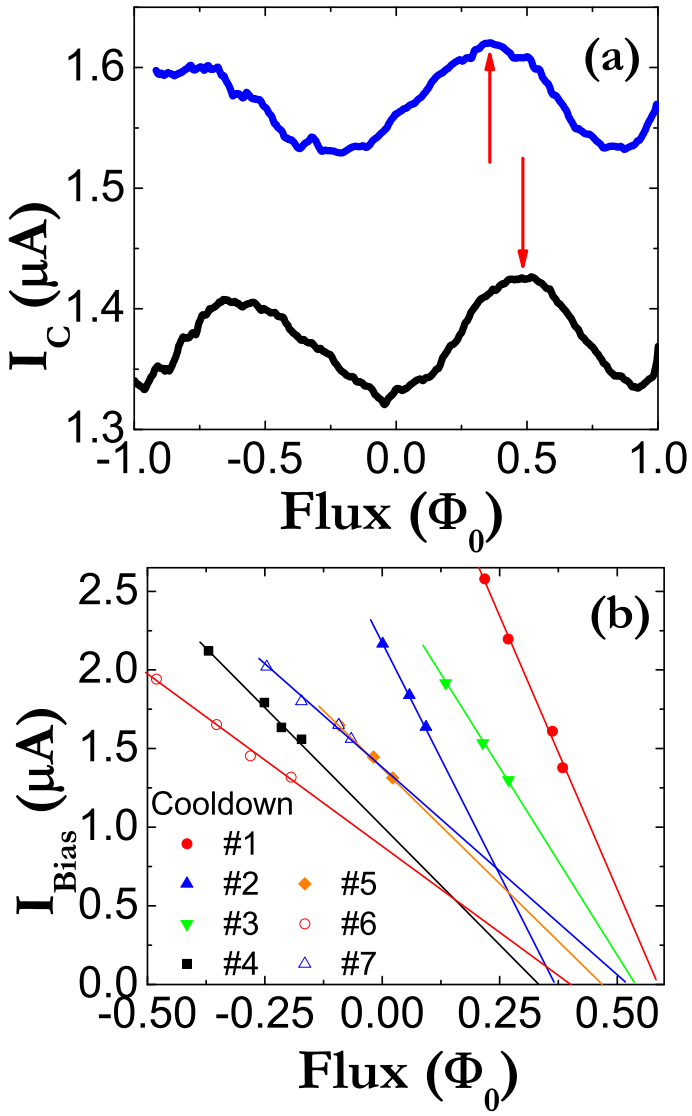

Figure 5.5: (a)Two SQUID modulation curves taken at 90mK with different bias currents - arrows denote the peaks and highlight the shift in position caused by asymmetric current flow. The arrow locations for these and other curves correspond to data points in plot (b). (b)Extrapolations to zero bias current for seven thermal cycles of the corner SQUID. The lines cluster around a phase shift of $0.5\Phi_0$.

In our case, each successive thermal cycle increased the apparent asymmetry between the junctions, flattening the extrapolation line. After removing the sample from the fridge, we noticed that the polyimide film was cracking along one crystal face. We believe that the effective contact width of one of the junctions was shrinking with each thermal cycle, but this does not affect our conclusions.

5.4 Discussion

We have made phase-sensitive measurements of the superconducting order parameter in UPt_3 with Josephson junctions fabricated on and around the corners of UPt_3 single crystals. The results show strong evidence that the order parameter in the low-temperature B-phase is complex and breaks time-reversal symmetry. Despite the similarity to Sr_2RuO_4, there was no sign of chiral superconducting domains. The data also indicate an intrinsic phase shift of π between the a- and b-axes, which supports the E_{2u} representation of the order parameter.

Chapter 6

Measuring the Angular Dependence of the Superconducting Order Parameter

In this chapter I present the results of measurements done on Josephson junctions fabricated on the surface of an as-grown UPt_3 crystal spanning a range of angles in the a-b plane. These measurements provide a picture of the shape of the superconducting gap amplitude and reveal the temperature dependence of the two components of the order parameter.

6.1 Motivation

Our previous study with UPt_3 strongly suggested that the superconducting order parameter matched the E_{2u} representation, but we wanted to perform another experiment to check our results. Rather than relying on the phase sensitivity of Josephson junctions, we decided to utilize their directionality to probe the magnitude of the superconducting energy gap and look for the precise location of nodes in the gap.

As previously mentioned, the tunneling probability of Josephson junctions drops off exponentially with barrier thickness so that a given junction effectively probes a single direction in k-space. The critical current of a Josephson junction between two superconductors depends on the amplitude of the order parameters and so a careful measurement of the critical current gives a direct measure of the order parameter for a given direction. This approach has been used successfully to map out the magnitude of the order parameter as a

function of angle in the cuprates, demonstrating their d-wave symmetry[48].

The E_{2u} representation also has a distinctive pattern of nodes in the order parameter that could be used to identify it. Even more interestingly, this nodal structure evolves with temperature because the E_{2u} model has two parts; a real component that turns on at T_{c+} and an imaginary component that turns on at T_{c-}, creating a complex order parameter state. This gives a temperature dependent gap that can be described by

$$\Delta(T) = \left|\Delta_R(T)(k_x^2 - k_y^2)k_z + \Delta_I(T)2ik_xk_yk_z\right| \tag{6.1}$$

where $\Delta_R(T)$ and $\Delta_I(T)$ are the temperature-dependent magnitudes of the real and imaginary components. The evolution of the order parameter with temperature is shown in Figure 6.1, where we have assumed a simple temperature dependence of the form $\Delta_R(T) \approx 1 - (T/T_{c+})^2$ and $\Delta_I(T) \approx 1 - (T/T_{c-})^2$; we will show that these functional forms are consistent with the data.

The primary feature that we will look for is the series of nodes in the high-temperature phase located 45° off the gap maxima. These gradually fill in as the out-of-phase component grows until the gap magnitude is isotropic in the zero-temperature limit. One interesting aspect of the nodes is that the four-fold symmetry of the order parameter differs from the hexagonal structure of the crystal lattice. This suggests that the order parameter might have degenerate configurations in which nodes would be locked in different directions separated by 30° in different domains or in successive cooldowns of the crystal. With this in mind, we fabricated Josephson junctions at a variety of angles around a single crystal of UPt_3, and measured the temperature dependence of the critical currents to map the evolution of the superconducting

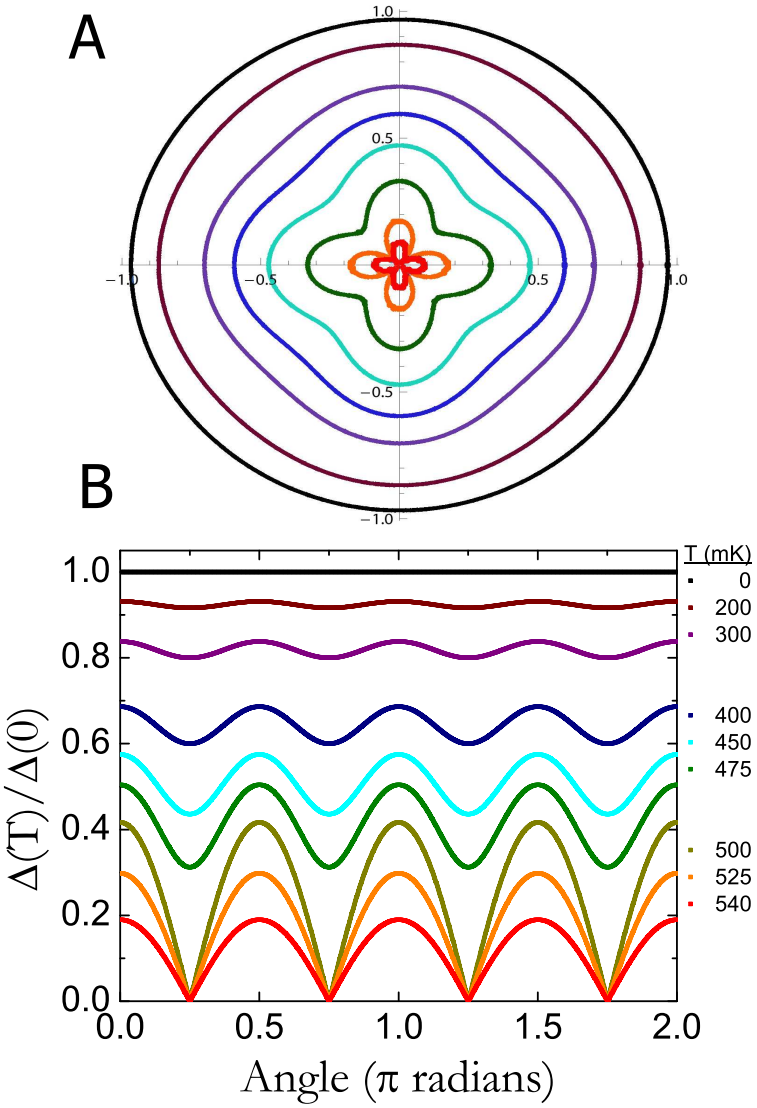

Figure 6.1: A - A 2-D cross-section of the superconducting energy gap amplitude, with the c-axis out of the page. Each line represents a different temperature, decreasing with distance from the origin. Note that the nodes in the high temperature phase gradually fill in as the low temperature component of the gap grows. B - The same profile of the energy gap amplitude plotted as a function of angle from the a-axis.

order parameter.

6.2 Experimental Details

The methods and equipment used in this experiment are nearly the same as those described in Chapter 4, but this section will describe the differences unique to this experiment. The samples used in this experiment were grown in the same manner as those used in the previous chapter, but rather than being polished to expose sharp corners for interferometry measurements, the as-grown surfaces were left untouched, although reference flats were still cut to identify the crystal axes. Using as-grown surfaces was important to ensure uniformity between junctions. We have observed that polishing the crystal can affect the surface and add to the effective thickness of the normal metal barrier, and it is difficult to make identical junctions in this fashion. The wafers cut out of the single-crystal rod were chosen so that the as-grown surface formed the circumference of the disk. The as-grown surface normal was tilted $\approx 3^\circ$ relative to the basal plane; this may be crucial for obtaining a finite critical current since evidence suggests that UPt_3 has a line node in the basal plane so that tunneling in the a-b plane should give zero critical current.

The gluing and masking techniques were identical to the previous work, but in the first crystal the junctions were spaced as evenly as possible around the available circumference of the disk. The resulting sample had eleven junctions that were approximately $50\mu m$ wide spanning 90° between the a- and b-axes. A picture of this sample can be seen in Figure 6.2.

In the case of the second crystal, a single extra-wide junction ($\approx 350\mu m$) was fabricated with its center 45° from the a-axis. Dry photoresist was used

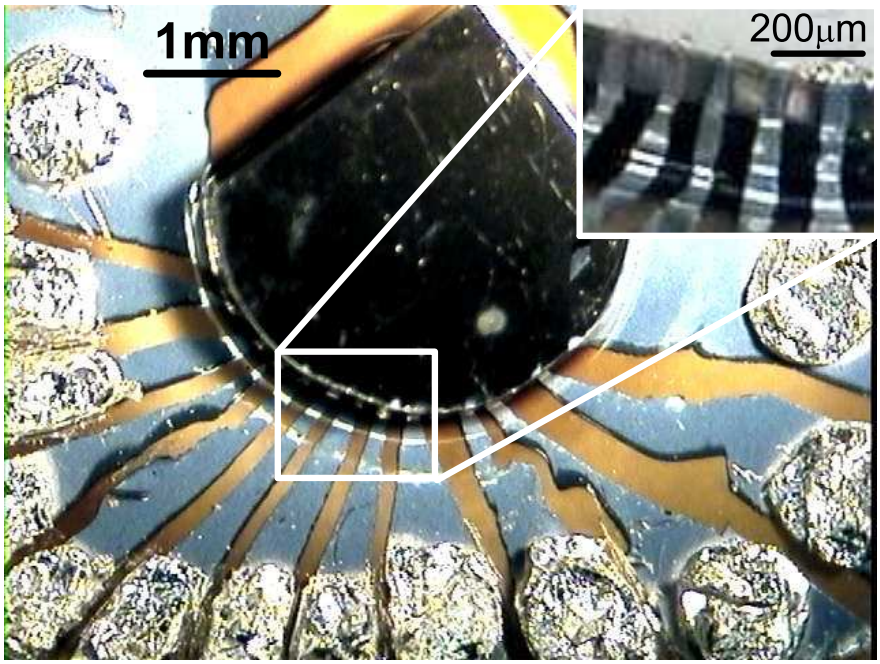

Figure 6.2: An overhead photograph of Sample 1. The large dark object is the UP_3 single crystal. The Pb electrodes and indium contact pads are also visible. The inset shows a portion of the crystal face with several junctions defined on its surface. All electrical contacts to the crystal were made on the as-grown face.

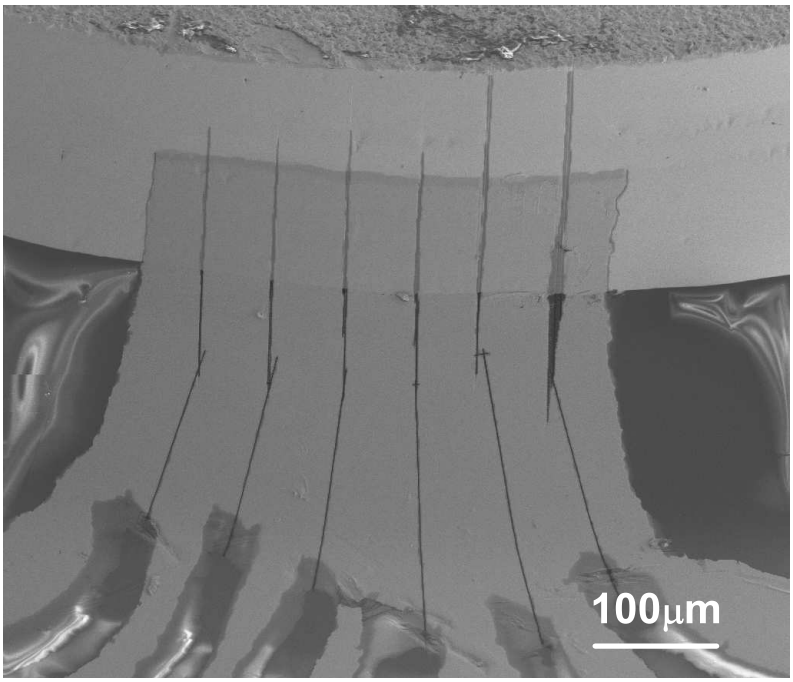

Figure 6.3: An SEM image of Sample 2. The bright region in the upper portion of the image is the as-grown crystal surface. The slightly darker junctions can be seen on top of the crystal, separated by the dark lines cut by the FIB.

to define electrical leads coming as close as possible to the crystal face without causing the strips of photoresist to touch. A Focused Ion Beam (FIB) was then used to cut the single large junction into seven smaller junctions, and then to connect those junctions to the electrical leads defined earlier. The seven small junctions were nearly identical in size to the junctions on the first sample, but the spacing between them was only $1\mu m$. This meant that the angular resolution of these junctions was substantially greater in the vicinity of the expected node in the superconducting order parameter. A Scanning Electron Microscope (SEM) image of these junctions can be seen in Figure 6.3.

6.3 Results

We measured the critical current as a function of temperature for each of our junctions, paying particular attention to the temperatures T_{onset} at which supercurrents first appeared. This data is presented in Figure 6.4A. We found that supercurrents onset just below the bulk superconducting transition T_{c+} for junctions at all angles except those very near 45° from the a-axis (±3°). For those junctions, the onset of supercurrent did not occur until near the lower transition T_{c-}. The angular dependence of T_{onset} is shown in Figure 6.4B. This sharp dip in T_{onset} confirms the location of a line node in the superconducting energy gap of the high-temperature component of the order parameter, which provides further verification of the E_{2u} symmetry picture. For each sample, the data were reproducible over several thermal cycles, with changes in T_{onset} for any given junction of less than $1mK$.

We found that the location of the node never changes in successive cooldowns on the sample. It is somewhat surprising that the location of the node never changes, because it might be expected that the order parameter should be able to choose between several degenerate options during each cooldown due to the different symmetries of the order parameter and the crystal lattice. Both the observations reported here and our previous interferometer experiment suggests that UPt_3 only forms a single superconducting domain[47]. We speculate that because the superconductivity is likely related to the antiferromagnetism in the crystal, this connection is also responsible for the order parameter alignment. If some factor such as a residual external magnetic field is aligning the magnetic moments, that could also impose a specific orientation to the order parameter. It is also possible that boundary conditions such as the reference flats cut into the crystal are providing a preferred

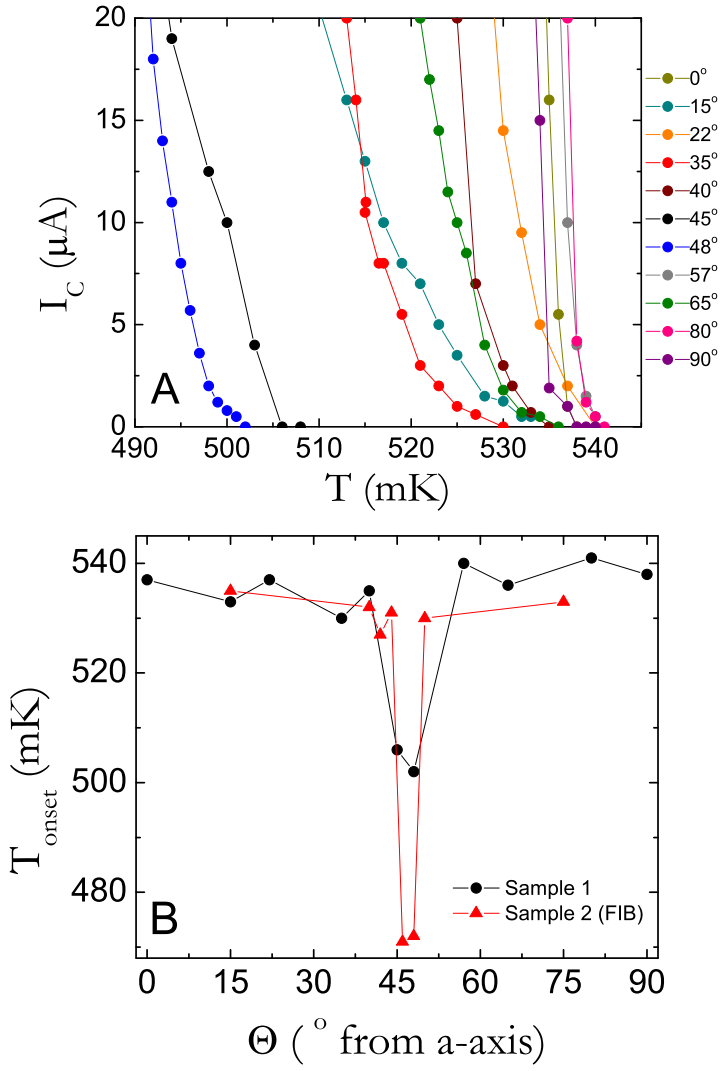

Figure 6.4: A - Plots of the critical current vs. temperature for Josephson junctions fabricated on the as-grown surface of Sample 1. B - The onset temperature for supercurrents vs. the angle (measured from the *a*-axis) of the junctions. The sharp dip at 45° indicates the presence of a node in the high-temperature component of the superconducting gap.

orientation of the order parameter. Further tests on samples without reference flats and during field cooling would have to be performed to clarify this issue.

In addition to the variation in onset temperature for supercurrents, we also found that the shape of the temperature dependence curves for critical currents varied with angle, as shown in Figure 6.5A. The rate of increase of the critical current is slower the closer the junction is to the node at 45°, but there is always a finite supercurrent that onsets near T_{c+} unless the junction is actually at the node. If the junction is close to the node, the rate of increase in critical current changes abruptly at T_{c-}, revealing the onset of the imaginary order parameter phase. This second phase increases the pairing amplitude and hence the critical current. We modeled this behavior with the E_{2u} representation of the gap magnitude from Equation 6.1 assuming that $I_c(T) \approx \Delta(T)$. We find that this model captures most of the features of our data using the temperature dependences assumed in Figure 6.1, namely $\Delta_R(T) \approx 1-(T/T_{c+})^2$ and $\Delta_I(T) \approx 1-(T/T_{c-})^2$. A comparison of our data with a simulation using this model can be found in Figure 6.5. This shows that we can observe not just the presence or absence of a gap, but also the angular dependence of the gap magnitude. In particular, there is a strong signature of the low-temperature component even at angles well away from the node.

These simulations also fit well with our data on junctions that were fabricated on surfaces polished with $0.3\mu m$ diamond lapping films prior to evaporation of the metal films. In those junctions, as with measurements by other groups on polished UPt_3 samples[49], we observed a linear increase of critical current as we lowered the temperature, with a distinct kink in the slope near T_{c-} that we attribute to the onset of an out-of-phase component at this

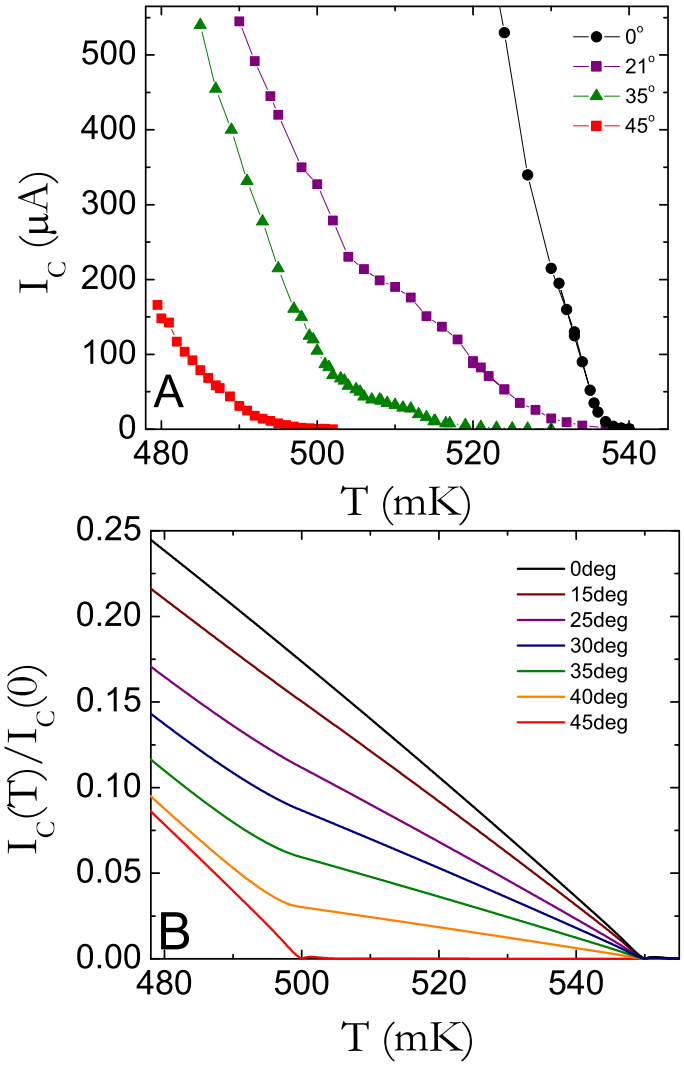

Figure 6.5: A - Data for a series of $I_c(T)$ curves for junctions fabricated at different angles in the basal plane. The magnitude grows more slowly for greater angles, but the onset temperature remains the same for all angles other than 45°. A kink in the slope can also be observed near T_{c-}. B - A simulation of $I_c(T)$ curves for two energy gaps with different onset temperatures, one with nodes and one without. The simulations give the same behavior we observed in our data.

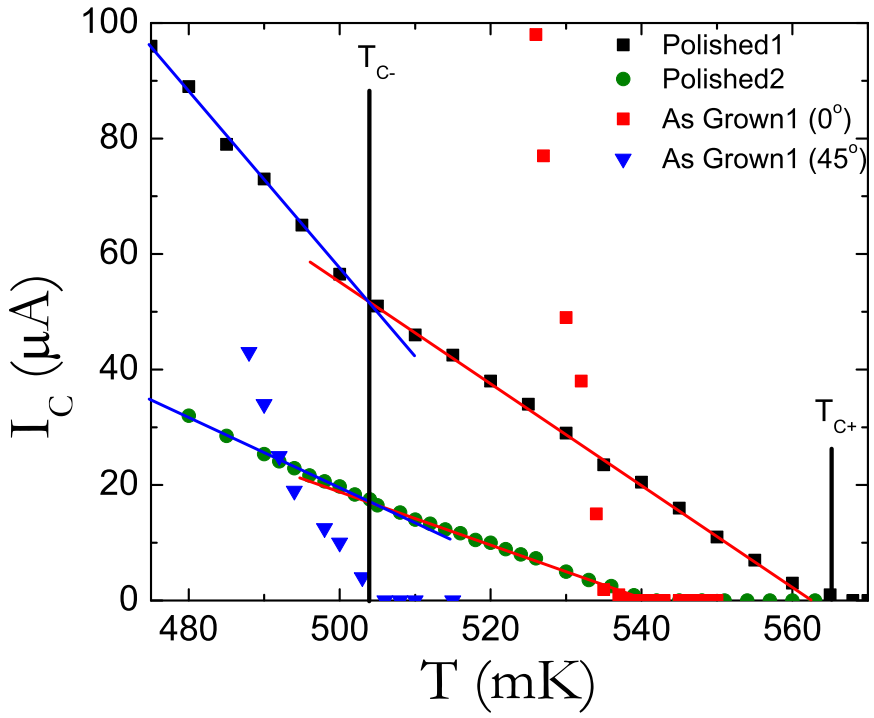

Figure 6.6: The $I_c(T)$ curves for two junctions fabricated on polished faces (nominally on the a-axis), as well as two junctions from the as-grown surface of Sample 1. The change in slope of the polished curves occurs at T_{c-}, where the second component of the order parameter turns on. This suggests that polishing causes more mixing of momentum states than with as-grown surfaces.

temperature. This sign of the second transition is surprising, since our junctions were nominally along the a-axis where we would expect to probe only a maximum of the order parameter. However, it has been established that polishing distorts the lattice at the surface of UPt_3[50], which could affect the directionality of the tunneling current. This mixing of momentum states could give signatures of multiple angles within a single junction. The data from these polished junctions is displayed in Figure 6.6.

In conclusion, we have fabricated S-N-S Josephson junctions on the as-grown surfaces of single crystals of UPt_3, spanning the angles between the a- and b-axes. By measuring the temperature dependence of the critical current through these junctions, we have observed the evolution of the angular

dependence of the superconducting gap magnitude. This demonstrates the existence of real and imaginary components that turn on at different temperatures, creating two distinct superconducting phases, a high-temperature real phase and a low-temperature complex order parameter phase. The results give us a clear picture of the relative magnitudes and symmetries of the two phases and the transition between them. They also reveal the presence of a line node in the high-temperature component at 45°, verifying the E_{2u} representation of the order parameter.

Chapter 7

Conclusions and Future Work

The heavy fermion superconductor UPt_3 provides a rich system for studying the competition between superconductivity and other forms of electronic order because it exhibits unconventional pairing, coexistence of anti-ferromagnetism and superconductivity, and two distinct superconducting phases characterized by different order parameter symmetries. In this thesis we presented data on the modulation of the critical current with applied magnetic field in UPt_3–Cu–Pb Josephson junctions and SQUIDs. The junctions were fabricated on polished surfaces of UPt_3 single crystals and the shape of the resulting diffraction patterns provided phase-sensitive information on the superconducting order parameter. Our corner junction data showed asymmetric patterns with respect to magnetic field, indicating a complex order parameter, and both our junction and SQUID measurements pointed to a phase shift of π within the crystal between the a- and b-axes, supporting the E_{2u} representation of the order parameter.

We also fabricated a series of Josephson tunnel junctions on the as-grown surfaces of UPt_3 single crystals spanning the a- and b-axes. By measuring their critical current, we mapped out the magnitude of the superconducting order parameter as a function of k-space direction and temperature. We observed a sharp node in the superconducting gap at 45° with respect to the a-axis and the onset of an out-of-phase component creating a complex order parameter in the low-temperature phase. These measurements also provided

evidence for the E_{2u} representation and triplet pairing symmetry.

All of these data help clarify the complicated nature of superconductivity in UPt_3, but there are several interesting features that have yet to be resolved. Most of our measurements were performed on junctions lying on or very near the basal plane, where it is generally believed there is a line node in the energy gap in both superconducting phases. If there is a node in the basal plane, then it should be impossible for us to tunnel into the UPt_3 crystal. As we noted in Chapter 6, the as-grown surface normal was a few degrees off of the basal plane, and given the sharpness of the node perpendicular to the basal plane it is possible that this tilt was sufficient to give a finite supercurrent. We also observed blending of momentum states in polished junctions, so our data in Chapter 5 could be explained by that phenomenon. It is also possible, however, that there is no basal plane node, which has been suggested by some recent thermal conductivity measurements[51]. If true, this would require significant alterations to the prevailing theories for superconductivity in UPt_3. This is an excellent motivation for another angle-dependence experiment studying junctions made on an as-grown surface in the a-c plane. In conjunction with this, phase-sensitive measurements looking for a sign change in the order parameter between $+z$ and $-z$ would be very enlightening.

The other oddity we discovered was the robust single orientation of the superconducting order parameter. We observed that the order parameter appeared to form a single domain across the entire crystal, and that it always chose the same orientation, despite having a different symmetry than the crystal lattice. As mentioned in Chapter 6, it is possible that some alignment of the antiferromagnetic moments in the crystal are providing a preferred orientation for the superconducting order parameter or that boundary

conditions of the crystal itself are imposing a direction. It would be interesting to perform tests on a sample without reference flats as well as cooling the samples in a magnetic field to change the alignment of the antiferromagnetic moments.

UPt_3 has been puzzling physicists for 25 years, and has enough complexity to ensure continued study for many more, but the measurements reported in this thesis have shed light on the pairing symmetry and shape of the superconducting order parameter in this very unconventional material.

References

[1] H. Onnes, *Comm. Phys. Lab. Univ. Leiden*, vol. 124c, 1911.

[2] V. Ginzburg and L. Landau, *Zh. Eksperim. Teor. Fiz.*, vol. 20, p. 1064, 1950.

[3] J. Bardeen, L. Cooper, and J. Schrieffer, *Phys. Rev. Lett.*, vol. 108, p. 1175, 1957.

[4] L. Gor'kov, *Zh. Eksperim. Teor. Fiz.*, vol. 34, p. 735, 1958.

[5] D. Walko, J. Hong, T. Chandrasekhar Rao, Z. Wawrzak, D. Seidman, W. Halperin, and M. Bedzyk, *Phys. Rev. B*, vol. 63, p. 054522, 2001.

[6] J. Chen, S. Lambert, M. Maple, Z. Fisk, J. Smith, G. Stewart, and J. Willis, *Phys. Rev. B*, vol. 30, p. 1583, 1984.

[7] R. Joynt and L. Taillefer, *Rev. Mod. Phys.*, vol. 74, p. 235, 2002.

[8] G. R. Stewart, Z. Fisk, J. O. Willis, and J. L. Smith, *Phys. Rev. Lett.*, vol. 52, p. 679, 1984.

[9] C. Broholm, G. Aeppli, R. Kleiman, D. Harshman, D. Bishop, E. Bucher, D. Williams, E. Ansaldo, and R. Heffner, *Phys. Rev. Lett.*, vol. 65, p. 2062, 1990.

[10] G. Aeppli, E. Bucher, C. Broholm, J. Kjerns, J. Baumann, and J. Hufnagl, *Phys. Rev. Lett.*, vol. 60, p. 615, 1988.

[11] M. Aronson, T. Vorenkamp, Z. Koziol, A. de Visser, K. Bakker, J. Franse, and J. Smith, *J. Appl. Phys.*, vol. 69, p. 5487, 1991.

[12] P. Anderson, *Phys. Rev. Lett.*, vol. 3, p. 325, 1959.

[13] R. A. Fisher, S. Kim, B. F. Woodfield, N. E. Phillips, L. Taillefer, K. Hasselbach, J. Flouquet, A. L. Giorgi, and J. L. Smith, *Phys. Rev. Lett.*, vol. 62, p. 1411, 1989.

[14] K. Hasselbach, L. Taillefer, and J. Flouquet, *Phys. Rev. Lett.*, vol. 63, p. 93, 1989.

[15] R. Heffner and M. Norman, *Comm. Cond. Mat. Phys.*, vol. 17, p. 361, 1996.

[16] K. Izawa, Y. Nakajima, J. Goryo, Y. Matsuda, S. Osaki, H. Sugawara, H. Sato, P. Thalmeier, and K. Maki, *Phys. Rev. Lett.*, vol. 90, p. 117001, 2003.

[17] S. Adenwalla, S. W. Lin, Q. Z. Ran, Z. Zhao, J. B. Ketterson, J. A. Sauls, L. Taillefer, D. G. Hinks, M. Levy, and B. K. Sarma, *Phys. Rev. Lett.*, vol. 65, p. 2298, 1990.

[18] B. Shivaram, Y. Jeong, T. Rosenbaum, and D. Hinks, *Phys. Rev. Lett.*, vol. 56, p. 1078, 1986.

[19] K. Behnia, L. Taillefer, J. Flouquet, D. Jaccard, K. Maki, and Z. Fisk, *J. Low Temp. Phys.*, vol. 84, p. 261, 1991.

[20] B. Lussier, B. Ellman, and L. Taillefer, *Phys. Rev. Lett.*, vol. 73, p. 3294, 1994.

[21] M. R. Norman and P. J. Hirschfeld, *Phys. Rev. B*, vol. 53, p. 5706, 1996.

[22] H. Suderow, J. P. Brison, A. Huxley, and J. Flouquet, *J. Low Temp. Phys.*, vol. 108, p. 11, 1997.

[23] L. Hebel and C. Slichter, *Phys. Rev.*, vol. 113, p. 1504, 1959.

[24] Y. Kohori, H. Shibai, T. Kohara, Y. Oda, Y. Kitaoka, and K. Asayama, *J. Mag. Mag. Mat.*, vol. 76, p. 478, 1988.

[25] H. Tou, Y. Kitaoka, K. Asayama, N. Kimura, Y. Onuki, E. Yamamoto, and K. Maezawa, *Phys. Rev. Lett.*, vol. 77, p. 1374, 1996.

[26] G. M. Luke, A. Keren, L. P. Le, W. D. Wu, Y. J. Uemura, D. A. Bonn, L. Taillefer, and J. D. Garrett, *Phys. Rev. Lett.*, vol. 71, p. 1466, 1993.

[27] P. D. de Reotier, A. Huxley, A. Yaouanc, J. Flouquet, P. Bonville, P. Imbert, P. Pari, P. Gubbens, and A. Mulders, *Phys. Lett. A*, vol. 205, p. 239, 1995.

[28] S. Hayden, L. Taillefer, C. Vettier, and J. Flouquet, *Phys. Rev. B*, vol. 46, p. 8675, 1992.

[29] K. Machida and M. Ozaki, *Phys. Rev. Lett.*, vol. 66, p. 3293, 1991.

[30] T. Ohmi and K. Machida, *Phys. Rev. Lett.*, vol. 71, p. 625, 1993.

[31] K. A. Park and R. Joynt, *Phys. Rev. B*, vol. 53, p. 12346, 1996.

[32] W. C. Wu and R. Joynt, *Phys. Rev. B*, vol. 65, p. 104502, 2002.

[33] J. A. Sauls, *Adv. in Phys.*, vol. 43, p. 113, 1994.

[34] M. J. Graf, S. Yip, and J. A. Sauls, *Phys. Rev. B*, vol. 62, p. 14393, 2000.

[35] B. Josephson, *Phys. Lett.*, vol. 1, p. 251, 1962.

[36] M. Tinkham, *Introduction to Superconductivity*, 2nd ed. Dover, 1996.

[37] J. R. Waldram, *Superconductivity of Metals and Cuprates*, 1st ed. Institute of Physics Publishing, 1996.

[38] D. J. Van Harlingen, *Rev. Mod. Phys.*, vol. 67, p. 515, 1995.

[39] D. A. Wollman, D. J. Van Harlingen, W. C. Lee, D. M. Ginsberg, and A. J. Leggett, *Phys. Rev. Lett.*, vol. 71, p. 2134, 1993.

[40] D. A. Wollman, D. J. Van Harlingen, J. Giapintzakis, and D. M. Ginsberg, *Phys. Rev. Lett.*, vol. 74, p. 797, 1995.

[41] F. Kidwingira, J. D. Strand, D. J. Van Harlingen, and Y. Maeno, *Science*, vol. 314, p. 1267, 2006.

[42] K. D. Nelson, Z. Q. Mao, Y. Maeno, and Y. Liu, *Science*, vol. 306, p. 1151, 2004.

[43] J. B. Kycia, B. Davis, J. Hong, M. Meisel, D. Seidman, and W. Halperin, *J. Low Temp. Phys.*, vol. 101, p. 623, 1995.

[44] H. Kambara, T. Yoshizumi, T. Mamiya, N. Kimura, R. Settai, E. Yamamoto, Y. Haga, and Y. Onuki, *Europhys. Lett.*, vol. 36, p. 545, 1996.

[45] A. Sumiyama, R. Hata, Y. Oda, N. Kimura, E. Yamamoto, Y. Haga, and Y. Onuki, *Phys. Rev. B*, vol. 72, p. 174507, 2005.

[46] E. Schuberth, G. Hofmann, F. Gross, K. Andres, and J. Hufnagl, *Europhys. Lett.*, vol. 11, p. 249, 1990.

[47] J. D. Strand, D. J. Van Harlingen, J. B. Kycia, and W. P. Halperin, *Phys. Rev. Lett.*, vol. 103, p. 197002, 2009.

[48] H. Smilde, A. Golubov, Ariando, G. Rijnders, J. Dekkers, S. Harkema, D. Blank, H. Rogalla, , and H. Hilgenkamp, *Phys. Rev. Lett.*, vol. 95, p. 257001, 2005.

[49] A. Sumiyama, S. Shibata, Y. Oda, N. Kimura, E. Yamamoto, Y. Haga, and Y. Onuki, *Phys. Rev. Lett.*, vol. 81, p. 5213, 1998.

[50] C. Obermair, G. Goll, H. v. Lohneysen, I. Yanson, and L. Taillefer, *Phys. Rev. B*, vol. 57, p. 7506, 1998.

[51] H. Shakeripour, C. Petrovic, and L. Taillefer, *New Journal of Physics*, vol. 11, p. 055065, 2009.